JOURNAL OF PETROLOGY

Journal of Petrology, 2020, Vol. 61, No. 9: egaa082
doi: 10.1093/petrology/egaa082
Advance Access Publication Date: 11 December 2020
Original Article

OXFORD

Evidence for Multi-stage Melt Transport in the Lower Ocean Crust: the Atlantis Bank Gabbroic Massif (IODP Hole U1473A, SW Indian Ridge)

Wei-Qi Zhang [1,2,3]*, Chuan-Zhou Liu[1,2,4,5], Henry J.B. Dick[3,6]

[1]State Key Laboratory of Lithospheric Evolution, Institute of Geology and Geophysics, Chinese Academy of Sciences, Beijing 100029, China; [2]University of Chinese Academy of Sciences, Beijing 100049, China; [3]Department. of Geology & Geophysics, Woods Hole Oceanographic Institution, Woods Hole Massachusetts 02543, USA; [4]Laboratory for Marine Geology, Qingdao National Laboratory for Marine Science and Technology, Qingdao 266061, China; [5]CAS Center for Excellence in Tibetan Plateau Earth Sciences, Beijing 100101, China; [6]State Key Laboratory of Marine Geology, Tongji University, Shanghai, 200092, China

*Corresponding author: Tel.: +86 010-82998001; fax: +86 010-62010846. E-mail: zwq@mail.iggcas.ac.cn

Received 15 March 2020; Accepted 30 July 2020

ABSTRACT

The architecture of lower oceanic crust at slow- and ultraslow-spreading ridge is diverse, yet the mechanisms that produce this diversity are not well understood. Particularly, the 660-km^2 gabbroic massif at Atlantis Bank (Southwest Indian Ridge) exhibits significant compositional zonation, representing a high magma supply end member for accretion of the lower ocean crust at slow and ultraslow-spreading ridges. We present the petrographic and geochemical data of olivine gabbros from the 809-metre IODP Hole U1473A at Atlantis Bank gabbroic massif. Structurally, the upper portion of U1473A consists of a ~600-metre shear zone; below this, the hole is relatively undeformed, with several minor shear zones. Olivine gabbros away from the shear zones have mineral trace element compositions indicative of high-temperature reaction with an oxide-undersaturated melt. By contrast, olivine gabbros within shear zones display petrographic and chemical features indicative of reaction with a relatively low-temperature, oxide-saturated melt. These features indicate an early stage of primitive to moderately evolved melt migration, followed by deformation-driven transport of highly evolved Fe–Ti-rich melts to high levels in this gabbroic massif. The close relationship between shear zones and the reaction with oxide-saturated melts suggests that syn-magmatic shear zones provide a conduit for late-stage, Fe–Ti-rich melt transport through Atlantis Bank lower crust. This process is critical to generate the compositional zonation observed. Thus, the degree of syn-magmatic deformation, which is fundamentally related to magma supply, plays a dominant role in developing the diversity of lower ocean crust observed at slow- and ultraslow-spreading ridges.

Key words: melt-rock reaction; oceanic crustal accretion; permeable melt transport; syn-magmatic deformation; ultraslow-spreading ridge

INTRODUCTION

Mid-ocean ridges generate vast majority of present-day magma on Earth, playing a major role in the thermal and chemical exchange between the crust, mantle, and surface reservoirs. Ultraslow-spreading ridges (spreading rate <20 mm/yr) comprise nearly 36% by length of all active spreading ridges, yet their composition and means of formation are poorly understood (Dick et al., 2003). Whereas fast-spreading ridges are typically thick (i.e. 4·5 km-thick), expose continuous lower oceanic crust (see reviews in Coogan (2014)) and possess axial melt lens near the dyke-gabbro transitions (e.g., Harding et al., 1989; Carbotte et al., 2013), ultraslow-spreading ridges are characterized by thin and often

© The Author(s) 2020. Published by Oxford University Press. All rights reserved. For permissions, please e-mail: journals.permissions@oup.com

Downloaded from https://academic.oup.com/petrology/article/61/9/egaa082/5890488 by Institute of Geology and Geophysics, CAS user on 04 March 2021

discontinuous crust (Dick et al., 2003), the absence of a well-defined axial melt lens (Detrick et al., 1990). Ultraslow-spreading regions may also be punctuated by localized melting anomalies, such as the Atlantis Bank melting anomaly at 57° to 61°E along the Southwest Indian Ridge (SWIR) (Yu & Dick, 2020).

Oceanic core complexes (OCC) exhume peridotites and cumulates via the low-angle detachment faulting, during the asymmetric spreading at slow- and ultraslow-spreading ridges (e.g., Cannat et al., 2006; Escartín et al., 2008; Smith et al., 2006; Tucholke et al., 1998). Geological observations and numerical modelling indicate that OCC form by long-lived detachment faulting over a range of melt supply where 30–50% of total extension at the plate boundary is accommodated tectonically (Olive et al., 2010; Tucholke et al., 2008). The Atlantis Bank OCC (SWIR) represents the high magma-supply end-member at which emplacement by long-lived, low-angle detachment faulting can occur (Dick, 1991; Dick et al., 2019a). Recent geological mapping of the Atlantis Bank gabbroic massif reveals it is both laterally and vertically zoned from primitive to highly evolved compositions, while extensive deep drilling showed it formed at moderate magma supply with extension at the plate boundary accommodated by a combination of intrusion, and crystal-plastic and brittle deformation (Dick et al., 2019a; Dick et al., 2019b). This contrasts to the gabbroic crust drilled at Atlantis Massif OCC (Mid-Atlantic Ridge, MAR) formed at relatively low melt magma supply, which shows no large-scale compositional zonation and experienced limited crystal-plastic deformation during its formation (Dick et al., 2019b; Godard et al., 2009; Suhr et al., 2008). The contrasting lower crustal structure between low and moderate melt supply OCCs suggests that ductile deformation of gabbroic crust can influence crustal architecture (Dick et al., 2019a, b; MacLeod et al., 2017).

Porous melt migration plays a major role in the generation of lower oceanic crusts (e.g., Coogan et al., 2000; Dick et al., 2019a; Ferrando et al., 2018; Gao et al., 2007; Lissenberg and Dick, 2008; Lissenberg et al., 2013; Leuthold et al., 2018) and to a large extent may dictate the composition of mid-ocean ridge basalts (MORB) (e.g., Collier and Kelemen, 2010; Lissenberg and Dick, 2008; Lissenberg et al., 2013; Lissenberg and Macleod, 2016). The occurrence of porous melt flow and melt-rock reaction within gabbroic crust is independent of spreading rates and magma supply (e.g., Coogan et al., 2000; Gao et al., 2007; Lissenberg et al., 2013); however, the driving forces of the porous melt flow within lower oceanic crust might vary dramatically with the spreading rates (e.g., Dick et al., 2019a; Lissenberg et al., 2013). Unlike fast-spreading ridges, the complex interplay between detachment faulting and magmatism can influence melt transport and reaction during the emplacement of OCC at slow- and ultraslow-spreading ridges (e.g., Brunelli et al., 2020; Dick et al., 1991; Natland et al., 2001; Sanfilippo et al., 2018; Tribuzio et al., 2020). Field evidence exemplifies this interplay; enrichments in oxide gabbros (e.g., Cannat et al., 1997; Dick et al., 1991; Sanfilippo et al., 2018) and felsic melt infiltration (Tribuzio et al., 2020) often occur in localized ductile shear zones within the gabbroic crusts. We seek to address a number of questions: (1) what is the role of ductile deformation on melt transport in thick lower ocean crust (i.e. Atlantis Bank); (2) how are melt transport and melt-rock reaction affected by deformation in olivine gabbros (major component of Atlantis Bank lower crust); and (3) can deformation and melt transport be related to gabbro composition and crustal architecture in a diagnostic way?

The 809-metre IODP Hole U1473A in the Atlantis Bank gabbroic massif (SWIR) provides a unique opportunity to decipher the multistage melt transport and the complex tectono-magmatic interplay during oceanic crustal accretion and, more broadly, provide constraints on the origin of diverse lower crustal architecture at slow- and ultraslow-spreading ridges. As the most abundant lithology of Atlantis Bank lower crust, olivine gabbro is the ideal lithology to investigate. Here we report the petrography and composition (bulk and mineral major and trace elements) of a suite olivine gabbros from different depths throughout Hole U1473A to evaluate these questions on a fine scale, from microns to hundreds of metres.

GEOLOGICAL BACKGROUND AND SAMPLES

The Atlantis Bank gabbroic massif is part of the Atlantis Bank OCC which flanks the Atlantis II Transform 73 km south of the modern axis of the ultraslow-spreading (14 mm/yr) SWIR (Fig. 1a–c). It intruded laterally into the mantle in the transform zone at the northern ridge-transform intersection from ~13 to 10·3 Ma, representing 2·7 Myr of lower crustal accretion (Dick et al., 2019a, b). During this time, it was continuously uplifted as it accreted into the southern rift mountains, exposing its contact with the mantle on the eastern transform wall (Dick et al., 2000, 2015, 2017; MacLeod et al., 2017). At this time, the SWIR was spreading ~9·8 mm/yr to the south and 4·9 mm/yr to the north, somewhat faster than at present (Baines et al., 2007, 2008). Detailed mapping and sampling coherently show that the outer parts of the Atlantis Bank gabbroic massif are characterized by the absence of primitive cumulates, namely dunite and troctolite, and an abundance of highly evolved oxide gabbros (Dick et al., 2019a, b). As the bulk compositions of these recovered cumulates are too evolved to be in equilibrium with even the most evolved MORB in this region, the presence of primitive cumulates (such as troctolite and dunite) in its core are inferred to balance the crust back to a primary magma (Fig. 1d) (Dick et al., 2000; Natland & Dick, 2001). Therefore, the Atlantis Bank gabbroic massif was proposed to be vertically and laterally zoned, from primitive gabbros/troctolites at its core to highly evolved oxide gabbros at its margins (Dick et al., 2019a), although further drilling is required to confirm this. Notably, the Atlantis Bank coincides

Downloaded from https://academic.oup.com/petrology/article/61/9/egaa082/5890488 by Institute of Geology and Geophysics, CAS user on 04 March 2021

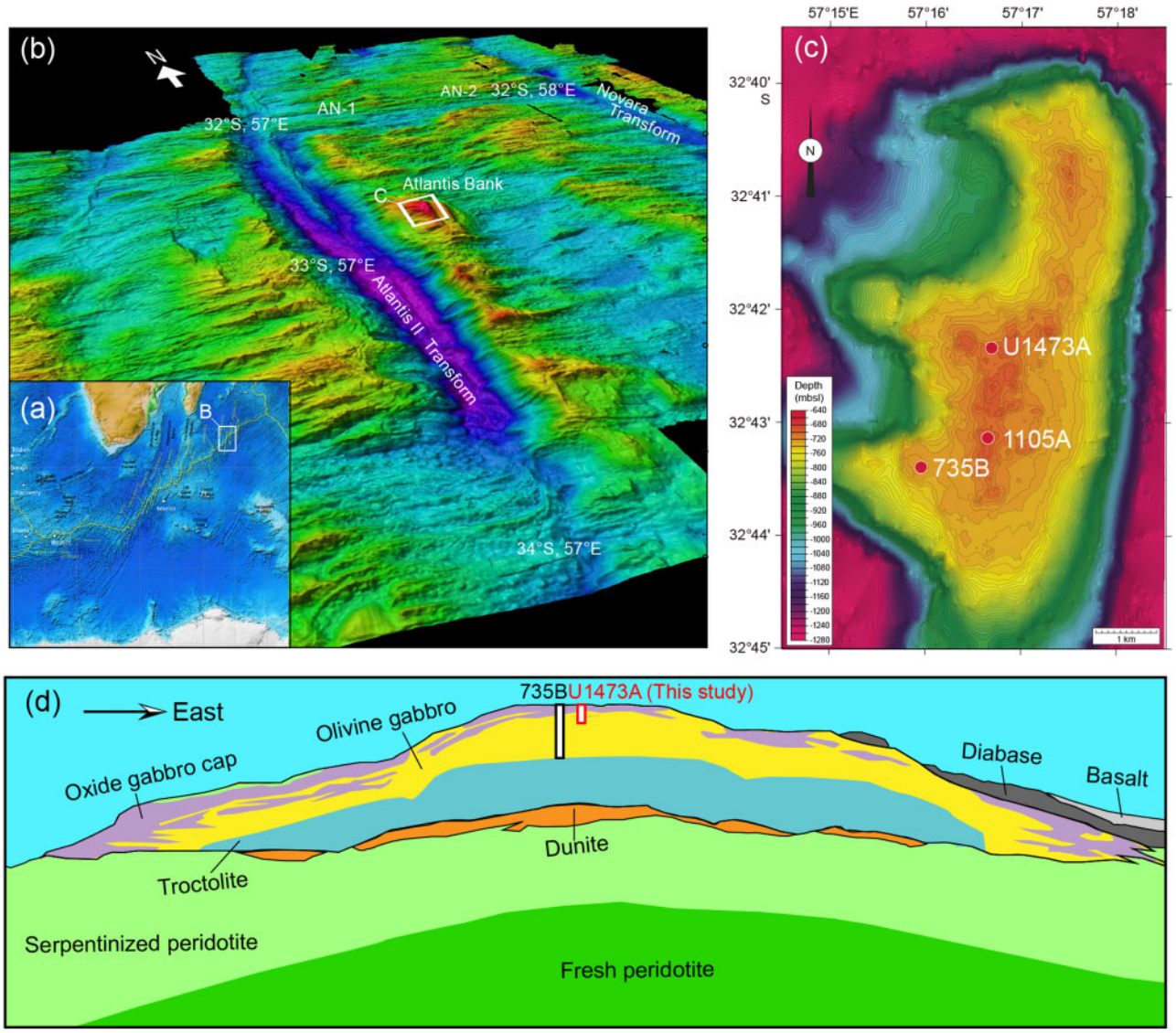

Fig. 1 (a) Topography of the Southwest Indian Ridge (SWIR) referred from Georgen et al. (2001). (b) Bathymetric map of Atlantis II Transform Fault, showing the location of Atlantis Bank gabbroic massif (Dick et al., 2017). (c) Bathymetric map of Atlantis Bank gabbroic massif, after Dick et al. (2017). (d) Inferred architecture of Atlantis Bank gabbroic massif after Dick et al. (2019a, b). Abbreviation: mbsl, metres below sea level.

with a mantle melting anomaly that began at ~14 Ma, and extended between the Atlantis II and Melville FZ (Yu & Dick, 2020), and thus represents an exceptionally robust SWIR magmatic regime.

Two ODP holes were previously drilled at Atlantis Bank: 1508 m Hole 735B and 157·4-m 1105A. The new 809-m IODP Hole U1473A, the focus of this paper, was drilled in 2015 and 2016 by Expeditions 360 and 362T (Fig. 1c) (Dick et al., 2000, 2015, 2017; MacLeod et al., 2017). Hole U1473A is composed volumetrically of 76·5 % olivine gabbro, 16·9 % oxide gabbro, 5·1% gabbro and 1·5% felsic veins (Fig. 2a) (Dick et al., 2017; MacLeod et al., 2017). There are numerous magmatic veins crosscutting the host olivine gabbros, including microgabbro, oxide gabbro and felsic veins. Microgabbro is characterized by a significant decrease in grain size (<1mm) compared with the host gabbroic rocks. Microgabbros include the entire range of lithologies, from troctolite, to olivine gabbro, gabbronorite and oxide gabbro. Oxide gabbro is characterized by an enrichment in Fe–Ti oxide (both ilmenite and magnetite) and other accessory mineral phases (brown amphibole, orthopyroxene, apatite and zircon). Felsic veins varying from diorite to tonalite are volumetrically minor, yet represent the most evolved component in Hole U1473A, (Dick et al., 2017; MacLeod et al., 2017).

The most remarkable structural feature of Hole U1473A is a pervasively deformed zone from 0– 589 mbsf (metres below seafloor), and several thin shear zones in a generally undeformed interval between 589 and 809 mbsf (Fig. 2b, c). The shear zones in the latter interval include two ~15–20m-thick zones at 620–635 and 668– 688 mbsf, and six smaller shear zones below 720 mbsf (Fig. 2b, c). Gabbros from this hole exhibit

Downloaded from https://academic.oup.com/petrology/article/61/9/egaa082/5890488 by Institute of Geology and Geophysics, CAS user on 04 March 2021

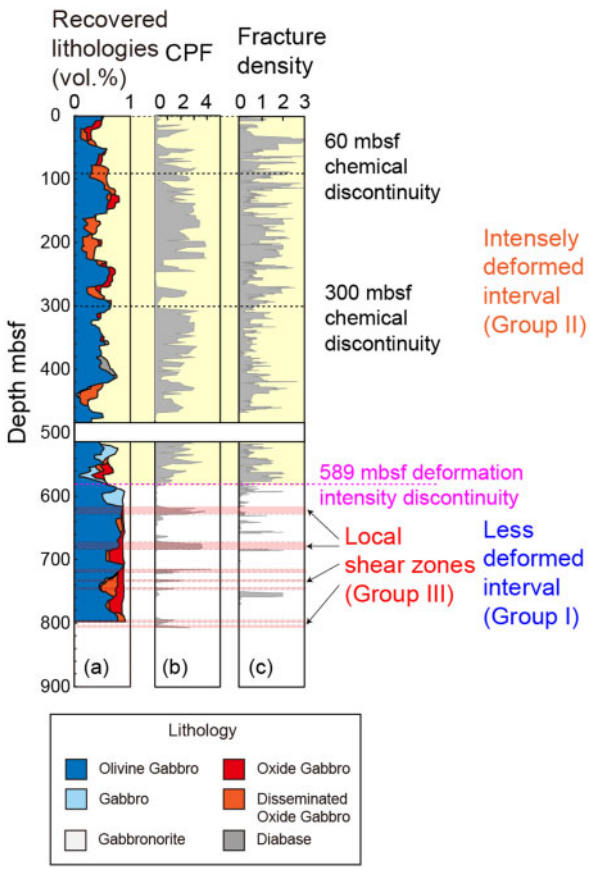

Fig. 2 Stratigraphic columns for IODP Hole U1473A. (a) Hole U1473A stratigraphic column representing 5-metre running average of the lithologic and unrecovered portions of the drilled intervals from MacLeod et al. (2017). (b) Crystal–plastic fabric intensity (CPF) averaged per 10 metres, from MacLeod et al. (2017). (c) Fracture density averaged per 11 cells (10 cm/cell): 1 - one fracture per 10 cm; 2 - two to five; 3 - greater than five from MacLeod et al. (2017). Red areas label the local shear zones below 589 mbsf. Black dashed lines represent the two chemical discontinuities at 90 and 300 mbsf. Pink dashed line marks the 589 mbsf deformation intensity discontinuity separating 0–589 mbsf shear zone and 589–809 mbsf less deformed interval. Abbreviation: mbsf, metres below seafloor.

various degree of ductile deformation with crystal–plastic fabric intensity varying from 0 to 5 (CPF: 0 - undeformed, 1 - foliated; 2 - porphyroclastic; 3 - protomylonite; 4 - mylonite; 5 - ultramylonite). Crystal–plastic foliations have variable dips, mostly ranging from 10–50°, without any systematic variation downhole (MacLeod et al., 2017). Amphibole, clay and carbonate veins are concentrated above 589 mbsf, and are rare in lower part of this hole (MacLeod et al., 2017). On the other hand, felsic veins and sulfides that record late-stage magmatic processes are mainly distributed in the 589–809 mbsf undeformed interval (Dick et al., 2017; MacLeod et al., 2017).

In this study, we selected 56 representative olivine-bearing gabbros from different depths throughout the lower oceanic crustal section recovered in IODP Hole U1473A (Fig. 2). A summary of crystal–plastic fabric intensity (CPF), mineral mode and mineral grain size for these 56 samples is provided in Table S1. All samples are coarse- to medium-grained olivine-bearing gabbros (Fig. S1a); fine-grained crosscutting microgabbros were excluded. Most samples are olivine gabbros with >5% olivine, >20% clinopyroxene, <1% orthopyroxene and <1% Fe–Ti oxides. Two are gabbros (15R-1W-112/116 and 25R-1W-93/100) with ~1% olivine and <1% Fe–Ti oxides. Two other samples (13R-1W-111/118 and 27R-3W-50/57) are disseminated oxide olivine gabbros with >1% Fe–Ti oxide (Fig. S1b). Sample 78R-2W-55/62 is a disseminated oxide olivine gabbronorite with >5% orthopyroxene, >1% Fe–Ti oxide and > 5% olivine. To simplify discussion, these are all named 'olivine gabbro' here.

Based on their respective spatial associations with shear zones, or lack thereof, the olivine gabbros are grouped into three types: Group I are from the undeformed 589–809-mbsf interval (Fig. 2), Group II the thick 0–589 mbsf sheared gabbro zone (Fig. 2) and Group III two small-scale ductile shear zones at 668–688 and 735–738 mbsf (Fig. 2). There are 29 Group I, 25 Group II and 2 Group III olivine gabbros.

PETROLOGY

Group I olivine gabbros are mostly undeformed and coarse- to medium-grained (e.g., Fig. 3a-c), with some having ophitic to poikilitic textures (Fig. 4a). They consist of plagioclase, clinopyroxene and olivine, with very minor interstitial orthopyroxene, Fe–Ti oxides (mainly ilmenite) and brown amphibole (Fig. S1b). Plagioclase occurs as euhedral to subhedral stumpy laths and anhedral grains, with local neoblast patches. Notably, fine- to medium-grained plagioclase grains can be enclosed by large clinopyroxene oikocryst with irregular contacts (Fig. 4a). Olivine occurs as intergranular to granular grains with rounded or irregular crystal shapes (Fig. 4b). Locally, corroded small olivine grains are enclosed by clinopyroxene or plagioclase with irregular contacts (Fig. 4c). Orthopyroxene generally occurs as interstitial phases filling the boundaries between olivine and plagioclase, commonly displaying irregular contacts (Fig. 4d). Plagioclase often contains deformation twins (Fig. 4e, f) and are locally bent (Fig. 4f). Grain boundaries between plagioclase grains are often irregular (see the red dashed lines in Fig. 4e, f) and are locally decorated with subgrains (Fig. 4e, f).

Group II olivine gabbros are characterized by intense crystal–plastic deformation (CPF= 1–4, at the thin-section scale), which is reflected in the dynamic recrystallization of primary minerals (e.g., Fig. 3d-f). They contain an average of 0·3 vol. % interstitial brown amphibole and 0·5 vol. % opaque minerals (ilmenite and sulfides), significantly higher than those of Group I gabbros (with mean values of 0·1 vol. % and 0·2 vol. %, respectively) (Fig. S1b). Primary clinopyroxene and olivine in Group II olivine gabbros display textures similar to Group I. Locally, clinopyroxene oikocrysts enclose plagioclase grains with irregular contacts (Fig. 5a).

Downloaded from https://academic.oup.com/petrology/article/61/9/egaa082/5890488 by Institute of Geology and Geophysics, CAS user on 04 March 2021

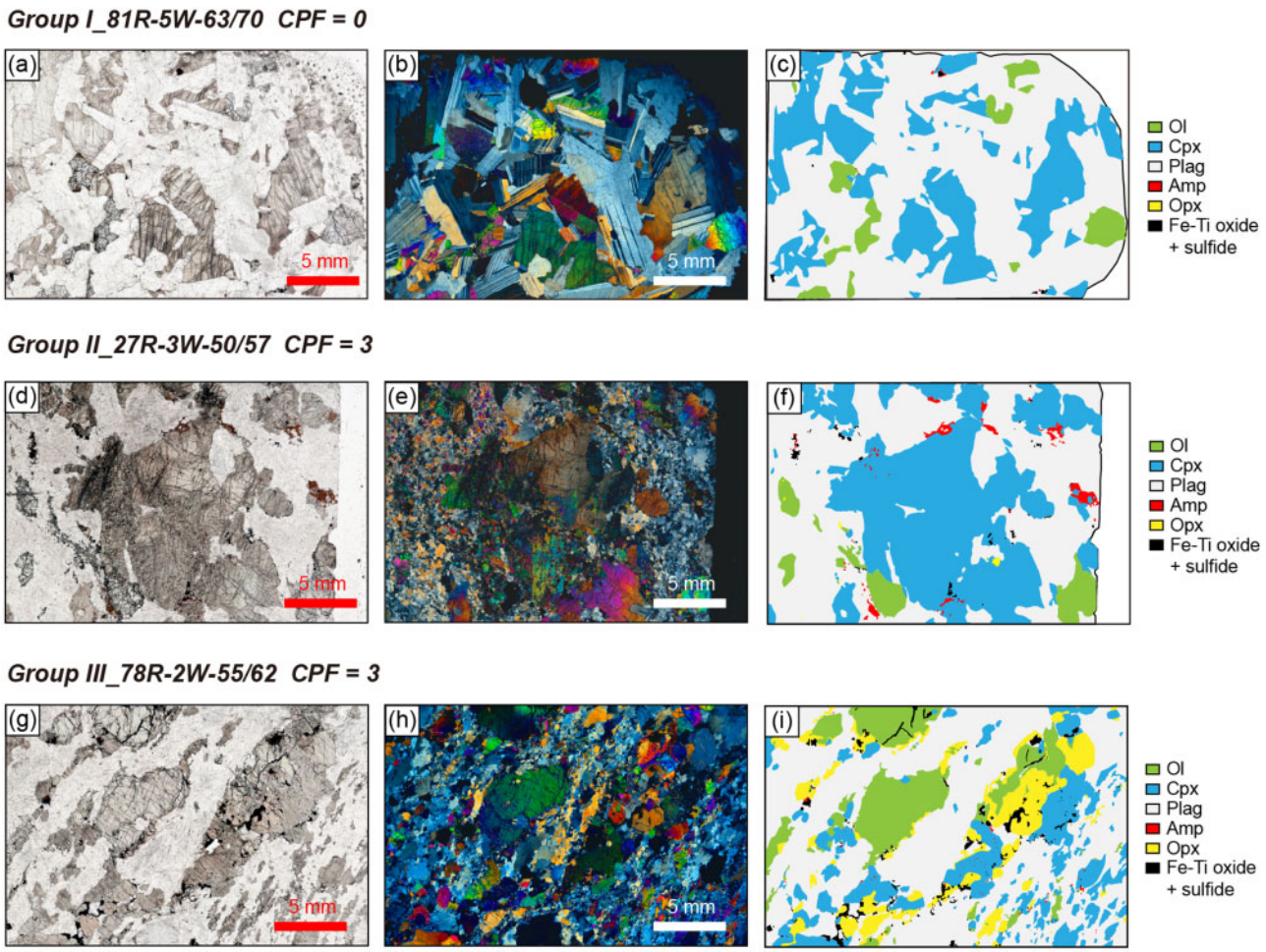

Fig. 3 Photomicrographs in transmitted plane-polarized light, cross-polarized light, and sketch illustration of Group I (a–c), II (d–f) and III (g–i) olivine gabbros. Abbreviations are as follows: Ol, olivine; Plag, plagioclase; Cpx, clinopyroxene; Opx, orthopyroxene; Amp, Amphibole, FTO, Fe–Ti oxide.

Primary clinopyroxene occurs as coarse grains with thin orthopyroxene exsolution lamellae. Olivine can locally occur as corroded small grains exhibiting lobate textures against large clinopyroxene grains (Fig. 5b). Orthopyroxene occurs as fine discontinuous grains mantling olivine, locally exhibiting resorbed textures (Fig. 5c). Ilmenite often exhibits irregular shapes and lobate contacts against the corroded olivine and plagioclase (Fig. 5d). Clinopyroxene and plagioclase commonly occur as corroded grains with lobate contacts against ilmenite (Fig. 5e). Aggregates of brown amphibole and ilmenite commonly fill the boundaries between neoblastic plagioclase and corroded clinopyroxene (Fig. 5f).

Compared to the Group I and Group II samples, Group III olivine gabbros are characterized by increased modal orthopyroxene, ilmenite and brown amphibole (Fig. S1b), and intense crystal–plastic deformation (CPF = 2–3). Group III olivine gabbros are porphyroclastic, and dynamic recrystallization of plagioclase is common (e.g., sample 78R-2W-55/62 in Fig. 3g-i). In less deformed sample 83R-6W-9/23 (CPF=2), olivine can occur as large oikocryst enclosing fine-grained plagioclase (Fig. 5g). Plagioclase and olivine are often present as highly corroded grains with lobate or irregular contacts against ilmenite (Fig. 5h). In sample 78R-2W-55/62, highly corroded olivine exhibits lobate contacts against the complex aggregates of orthopyroxene and clinopyroxene, and irregularly-shaped ilmenite (Fig. 5i).

METHODS

All measurements in this study were carried out at the Institute of Geology and Geophysics, Chinese Academy of Sciences (IGGCAS) in Beijing, China.

Mineral major and trace element chemistry

Only primary clinopyroxene, plagioclase, olivine and interstitial orthopyroxene rimming olivine were analysed for major and trace elements. Major elements were analysed on a JEOL JXA-8100 Electron Probe, using an accelerating voltage of 15 keV and a beam current of 10 nA. Trace element mineral compositions were determined *in-situ* by LA-HR-ICP-MS with a Thermo Scientific ELEMENT XR high-resolution ICP-MS

Downloaded from https://academic.oup.com/petrology/article/61/9/egaa082/5890488 by Institute of Geology and Geophysics, CAS user on 04 March 2021

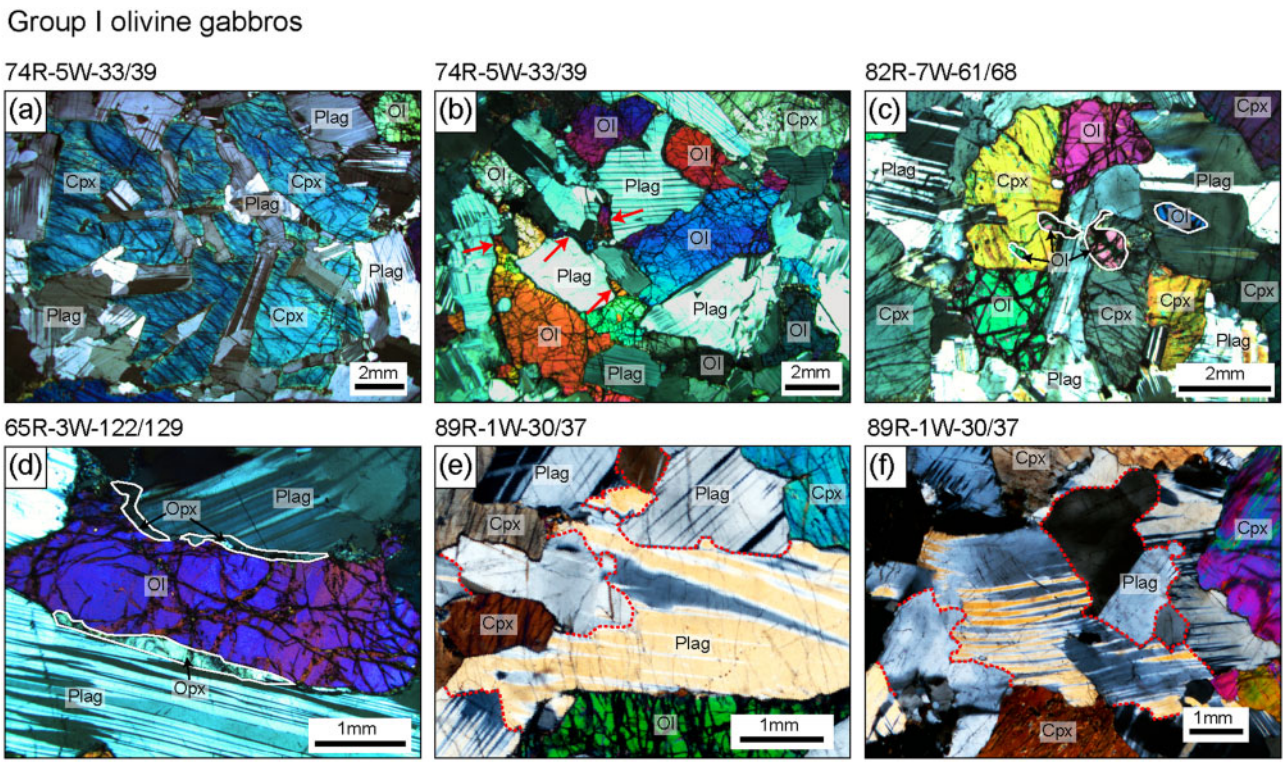

Fig. 4 Photomicrographs, in transmitted cross-polarized light, showing the textures of Group I olivine gabbros. (a) Plagioclase grains enclosed by a large clinopyroxene oikocryst with irregular contacts; (b) irregularly-shaped olivine exhibits resorbed texture against plagioclase; (c) highly corroded small olivine grains enclosed by clinopyroxene and plagioclase; (d) orthopyroxene interstitial to olivine and plagioclase; (e) plagioclase grain with deformation twins; (f) blended plagioclase with deformation twins. Abbreviations are as follows: Ol, olivine; Plag, plagioclase; Cpx, clinopyroxene; Opx, orthopyroxene.

coupled to a 193-nm Analyte G2 ArF Excimer laser, following the methods described in Wu et al. (2018a, b). Nitrogen was added to enhance sensitivity and helium was used as the carrier gas, and then mixed with argon gas before entering the plasma. For laser ablation, an energy density of 10–15 J/cm^2 and a frequency of 6 Hz were used. The beam size was set to 35 μm for clinopyroxene, 35 μm for plagioclase, 85 μm for olivine and 65μm for orthopyroxene. Visible cracks, fractures and inclusions were avoided during the measurements. Data were collected in time resolved acquisition mode, with background signal collected for 80s followed by 40s of sample ablation. The signals were collected for single spot analysis to monitor the potential fluid or mineral inclusion signals. ^{43}Ca (obtained by Electron Probe analysis) was used as an internal standard for both clinopyroxene and plagioclase, while ^{29}Si (obtained by Electron Probe analysis) was used for olivine and orthopyroxene. Raw data were reduced using the GLITTER 4·0 software (Griffin et al., 2008). The standard glass SRM NIST 612 was used as an external calibration standard to optimize the instrument sensitivity. The compositions of standard SRM NIST 612 are from Pearce et al. (1997). The standard glasses BCR-2 and GOR132 were analysed to determine precision and accuracy during measurement. The measured and preferred values of standards in this study are supplied in Table S2. The recommended standard values are from the GEOREM website (Jochum et al., 2005). Detection limits for most incompatible trace elements are lower than 1 ppb, but <5 ppb for Rb, Sr and Y. Measured values of most trace elements are identical to the preferred standard values within error (1 S.D.) of 15%. Rare earth element patterns were normalized to Sun & McDonough (1989). Mineral major and trace element data are given as mean compositions in Table S3 for olivine, Table S5 for clinopyroxene, Table S6 for plagioclase and Table S7 for orthopyroxene.

Whole-rock major and trace element chemistry

For whole-rock major and trace element analyses, the samples were selected to provide at least 100 g of material for whole-rock powders to make sure the chemical compositions of these powders are representative of the whole-rock compositions. Part of each sample was crushed to small fragments using plastic sheets with a rock hammer, and then the freshest parts were picked and powdered to 200 meshes in an agate mill. Whole-rock major elements were determined by X-ray Fluorescence (XRF) spectroscopy. About 0·5 g of sample powder was weighed and mixed with 5 g of $Li_2B_4O_7$. Loss on ignition (LOI) was measured by the weight difference before and after heating to 1000°C, before making the glass beads. The glass beads were analysed on an AXIOS Mineral Spectrometer, with ~1 to 3% analytical uncertainties (1 S.D.). According to the triplicate

Downloaded from https://academic.oup.com/petrology/article/61/9/egaa082/5890488 by Institute of Geology and Geophysics, CAS user on 04 March 2021

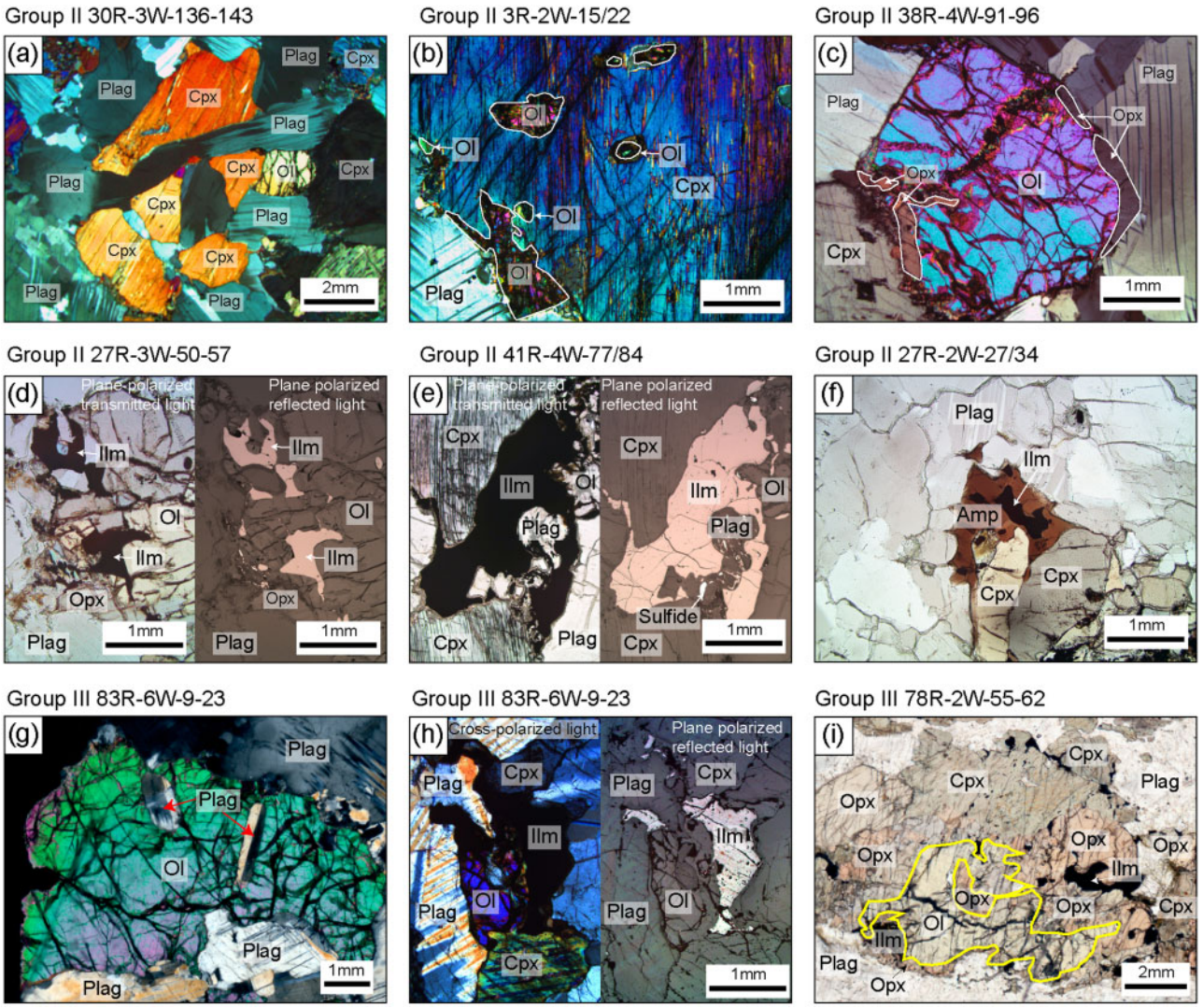

Fig. 5 Textures of Group II (a–f) and III (g–i) olivine gabbros. (a) Plagioclase chadacrysts enclosed by a clinopyroxene oikocryst; (b) relicts of corroded olivine grains in a large clinopyroxene grain; (c) orthopyroxene rimming olivine with straight or irregular contacts; (d) corroded olivine and plagioclase with lobate contacts against ilmenite and orthopyroxene; (e) corroded clinopyroxene and plagioclase with lobate contacts against ilmenite; (f) ilmenite and brown amphibole corona filling the boundaries between neoblastic plagioclase and corroded clinopyroxene; (g) plagioclase chadacrysts enclosed by a large olivine grain; (h) corroded olivine and plagioclase with lobate contacts against ilmenites; (i) highly corroded olivine showing lobate contacts against the complex aggregate of coarse-grained orthopyroxene, clinopyroxene and ilmenite. Abbreviations are as follows: Ol, olivine; Plag, plagioclase; Cpx, clinopyroxene; Opx, orthopyroxene; Ilm, ilmenite; Amp, brown amphibole.

measurements of USGS standard GSR-1, the 95% confidence limits for XRF measurements are ±0·04% to ±0·05% for SiO_2 and Al_2O_3, ±0·01% to ±0·02% for Fe_2O_3, MgO, Na_2O and K_2O and <±0·01% for TiO_2, MnO, CaO and P_2O_5, respectively. Trace element analysis was carried out using an Agilent 7500a mass spectrometer. Before analysis, ~50 mg sample powder was weighed, followed by mixing with HNO_3, HF and $HClO_4$ in Teflon bombs at 195°C for 4 days. The solution was evaporated and dissolved using HNO_3 to remove HF, before being mixed with HNO_3 at 195°C for ~8 hours. Then, the solutions were mixed with 1 g Rh internal standard and diluted to 100 g by adding ultra-clean water. Standards BCR-2 and BHVO-2 were analysed together with the samples, giving an analytical accuracy better than 5% for most trace elements. Whole-rock major and trace element data are given in Table S4.

RESULTS

Olivine

In this study, except for the profile analysis on two olivine grains (Fig. 6), we only analysed the olivine cores. Of the two olivine profiles conducted neither exhibit forsterite content ($Fo=100\times Mg/(Mg+Fe^{2+})$) zonation, e.g., 70R-4W-115/122 and 83R-6W-9/23 (Fig. 6b, g). Group I olivine gabbros have olivine Fo of 72–77 mol %, higher than Group II (Fo = 63–77 mol %) and Group III (Fo = 56–63 mol %). Olivine Fo is positively correlated with

Downloaded from https://academic.oup.com/petrology/article/61/9/egaa082/5890488 by Institute of Geology and Geophysics, CAS user on 04 March 2021

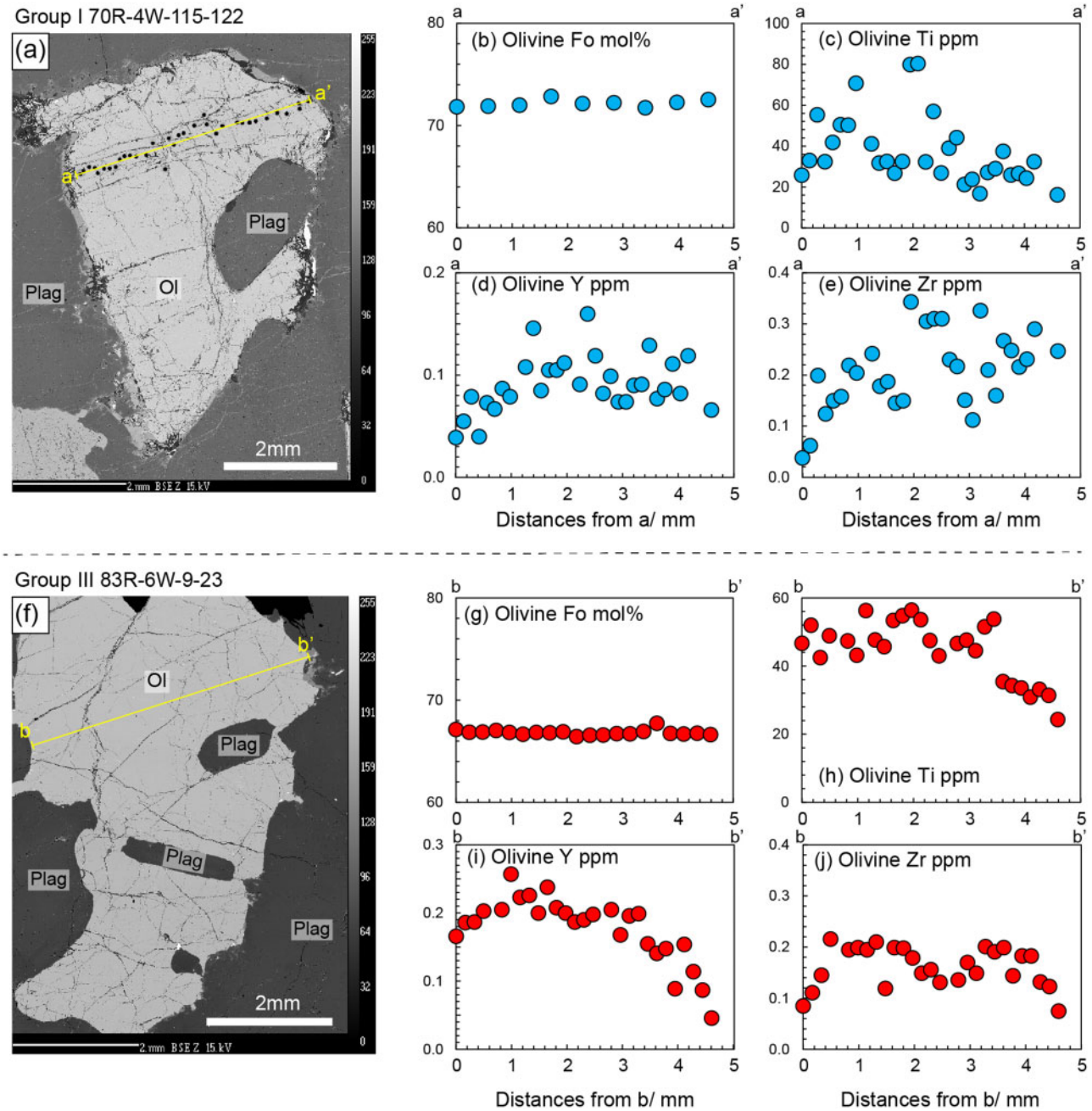

Fig. 6 Forsterite content (Fo), Ti, Y, and Zr compositional profiles across two olivine grains in sample 70R-4W-115/122 (a–e) and 83R-6W-9/23 (f–j). The back-scattered electron (BSE) images of the two olivine grains are given. Abbreviations are as follows: Ol, olivine; Plag, plagioclase; Cpx, clinopyroxene.

clinopyroxene Mg#, following the Fe–Mg equilibrium line (Fig. 7a). Clinopyroxene core Mg# are weakly correlated with olivine core Fo compared to clinopyroxene rim Mg# (Fig. 7a). In comparison, orthopyroxene Mg# displays a stronger correlation with olivine Fo than either the clinopyroxene rims or cores (Fig. 7b).

Olivine in all groups generally exhibits reverse heavy field strength element (HFSE) and heavy rare earth element (HREE) zonation (Fig. 6c–e, h–j). For instance, in sample 70R-4W-115/122, the Y and Zr contents in olivine can decrease from ~0·1 ppm to ~0·05 ppm and from ~0·2 ppm to ~0·05 ppm from cores to rims (a to a′), respectively (Fig. 6d, e). All olivine analysed displays comparable trace element patterns (Fig. 8a, b). They are relatively rich in HREE with Yb_N (CI-Chondrite normalized value) ranging from 0·06 to1·26, but highly depleted in medium rare earth element (MREE) (Dy_N=0·001–0·050) and light rare earth element (LREE) (Ce_N=0·0005–0·0081). Significant MREE/HREE fractionation is found, with Dy_N/Yb_N of 0·02–0·15, overlapping the range of olivine from Atlantis Massif (MAR) Hole U1309D olivine-rich troctolite (Dy_N/Yb_N = 0·04–0·11)

Downloaded from https://academic.oup.com/petrology/article/61/9/egaa082/5890488 by Institute of Geology and Geophysics, CAS user on 04 March 2021

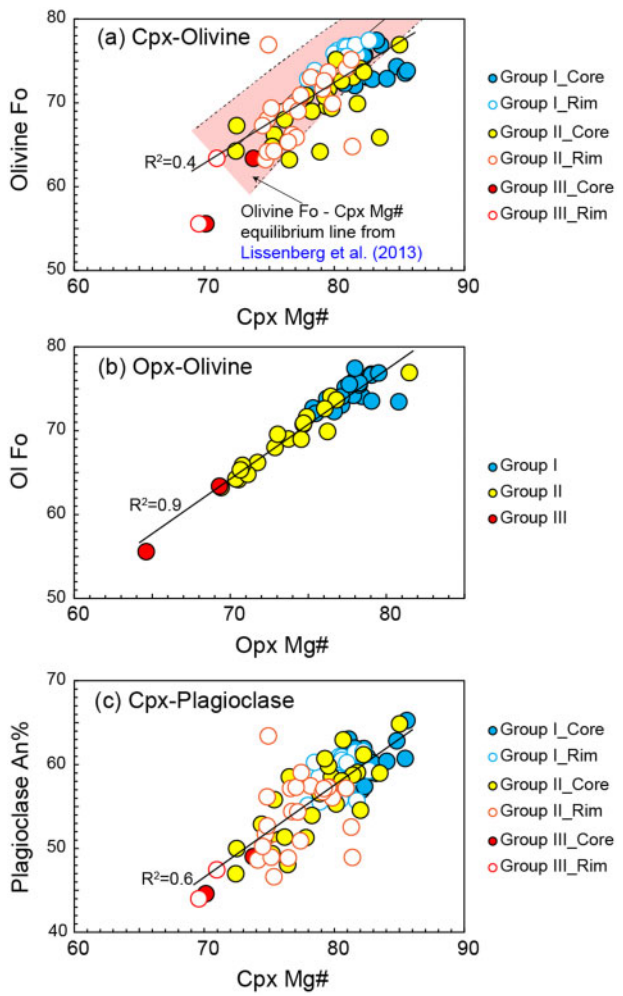

Fig. 7 (a) Olivine forsterite content (Ol Fo) vs clinopyroxene (Cpx) Mg# with the olivine- clinopyroxene Fe–Mg equilibrium line from Lissenberg et al. (2013), (b) Ol Fo vs orthopyroxene (Opx) Mg#, (c) Plagioclase anorthosite content (An%) vs clinopyroxene (Cpx) Mg#.

(Ferrando et al., 2018). For other trace elements, olivine exhibits positive anomalies of HFSE (e.g., Nb, Ta, Zr, Hf) and Y (Fig. 8a, b). They have Zr/Y ratios varying from 0·4 to 6·6, higher than the Hole U1309D olivine-rich troctolites [Zr/Y=0·1–1·0, from Ferrando et al. (2018)].

Olivine displays positive correlations between Ni and Fo, consistent with olivine from Hole 735B gabbros (Atlantis Bank, SWIR) and Hole U1309D cumulates (Atlantis Massif, MAR) (Fig. 9a). The Yb contents in olivine progressively increases with decreasing olivine Fo. Group I olivine gabbros have lower olivine Yb contents, and higher olivine Fo compared to Group II and III (Fig. 9b). Group I olivine exhibits a negative correlation between Ti and Fo, which has a steeper slope than those of Group II and III olivine (Fig. 9c). Group I olivine displays increasing Zr at decreasing forsterite content, defining the Zr–Fo correlations with steeper slopes than Group II and III (Fig. 9d). Group I olivine is represented by their high and variable Ti/Y and Zr/Y ratios, which is clear distinct with respect to Group II and III olivine which display low and uniform Ti/Y and Zr/Y ratios (Fig. 9e, f).

Clinopyroxene

Clinopyroxene in all groups is weakly zoned in Mg# ($=100\times Mg/(Mg+Fe^{2+})$), with slightly lower Mg# in rims with respect to cores (Fig. 10a). For instance, clinopyroxene in Group I olivine gabbros has normal Mg# zonation, with 80–86 mol % in the cores and 78–83 mol % in the rim. By contrast, Group II olivine gabbros have clinopyroxene Mg# close to Group I clinopyroxene, but display larger core to rim variations, with 72–85 mol % in the cores and 74–81 mol % in the rims. Group III clinopyroxene displays lower Mg# (i.e. Mg#=70–74 for cores and 70–71 for rims) than both Group I and Group II clinopyroxene. Clinopyroxene Mg# exhibit positive but scattered correlations with olivine forsterite contents (R^2=0·4, Fig. 7a) and plagioclase anorthite contents (R^2=0·6, Fig. 7c).

All clinopyroxene exhibit strong incompatible trace element zonation, with higher incompatible trace element contents in rims with respect to cores (e.g., TiO_2, Zr, Ce, and Y, Fig. 10b–e). All clinopyroxene have comparable trace element patterns, with LREE depletion with respect to MREE and HREE (La_N/Sm_N=0·08–0·28) (Fig. 8c, d). Cores generally display weak Eu anomalies (Eu/Eu*=0·84 in average, where $Eu/Eu^*=Eu_N^2/Sm_N\times Gd_N$), particularly compared to the strong negative Eu anomalies in clinopyroxene rims (Eu/Eu*=0·57 on average) (Fig. 8c, d). All clinopyroxene show prominent negative Sr and Ti anomalies (Fig. 8c, d). Note that clinopyroxene cores display negative Zr and Hf anomalies [Zr/Sm=0·2–0·8 × primitive mantle values (PM)]. In comparison, clinopyroxene rims (Zr/Sm=0·3–1·9 × PM), show weak negative to positive Zr and Hf anomalies (Fig. 8c, d).

Clinopyroxene in all groups is characterized by the increasing TiO_2 and Na_2O contents at decreasing Mg#, consistent with fractional crystallization trends (Fig. 11a, b). Clinopyroxene in Group I olivine gabbros displays relatively high Ti/Dy ratios (generally >800) and Mg# (i.e. Mg# > 78), similar to olivine gabbros from other oceanic ridges (Fig. 11c). By contrast, Group II and III olivine gabbros are characterized by a decrease in clinopyroxene Ti/Dy ratios (i.e. from ~1200 to ~500) with the decreasing clinopyroxene Mg#. Remarkably, the Group II clinopyroxene rims and all Group III clinopyroxene exhibit Ti/Dy – Mg# correlations indistinguishable from oxide gabbro-hosted clinopyroxene (Fig. 11c). Clinopyroxene in all olivine gabbros displays well-defined positive Ce–Y correlations (R^2=0·86), consistent with other oceanic gabbros (Fig. 11d).

Plagioclase

Most plagioclase is weakly zoned in anorthite contents [$An=100\times Ca/(Ca+Na)$] (Fig. 10f), with values ranging from 57 to 65 mol % for cores, and from 55 to 62 mol % for rims, while Group II plagioclase shows a larger

Downloaded from https://academic.oup.com/petrology/article/61/9/egaa082/5890488 by Institute of Geology and Geophysics, CAS user on 04 March 2021

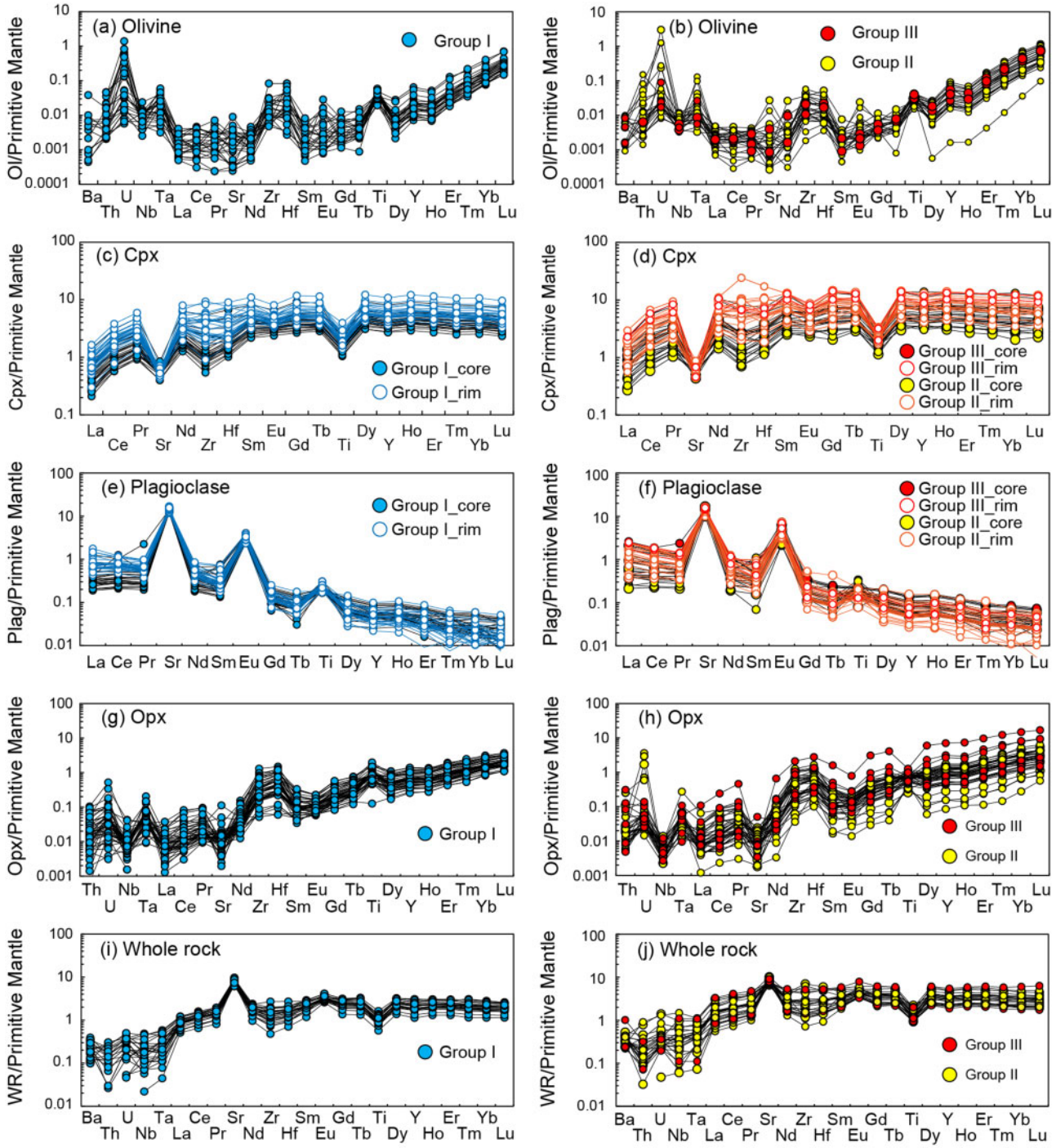

Fig. 8 Trace element patterns of olivines (Ol), clinopyroxenes (Cpx), plagioclases (Plag), orthopyroxenes (Opx), and whole rocks. Primitive Mantle values are from Sun and Mcdonough (1989).

compositional variation, from 47 to 65 mol % for cores and from 47 to 63 mol % for rims. Correlations between plagioclase anorthite content and clinopyroxene Mg# are scattered for both the core and rim pairs (R^2=0·6, Fig. 7c).

Group I plagioclase exhibits normal Ti zoning, with higher Ti contents in rims with respect to cores, whereas Group II and III plagioclase possess lower Ti abundances in rims than cores (Fig. 10g). Plagioclase in all groups have higher LREE (e.g., Ce) yet slightly lower Y contents in rims than cores (Fig. 10h, i). All plagioclase has comparable trace element patterns, with LREE enrichments compared to HREE, and prominent positive Eu and Sr anomalies (Fig. 8e, f).

Group I plagioclase exhibits negative correlations between Ti/Y ratios and anorthite content, with mean Ti/Y ratios of 2351±922 (Fig. 11e). In comparison, Group II and III plagioclase displays low and uniform Ti/Y ratios

Downloaded from https://academic.oup.com/petrology/article/61/9/egaa082/5890488 by Institute of Geology and Geophysics, CAS user on 04 March 2021

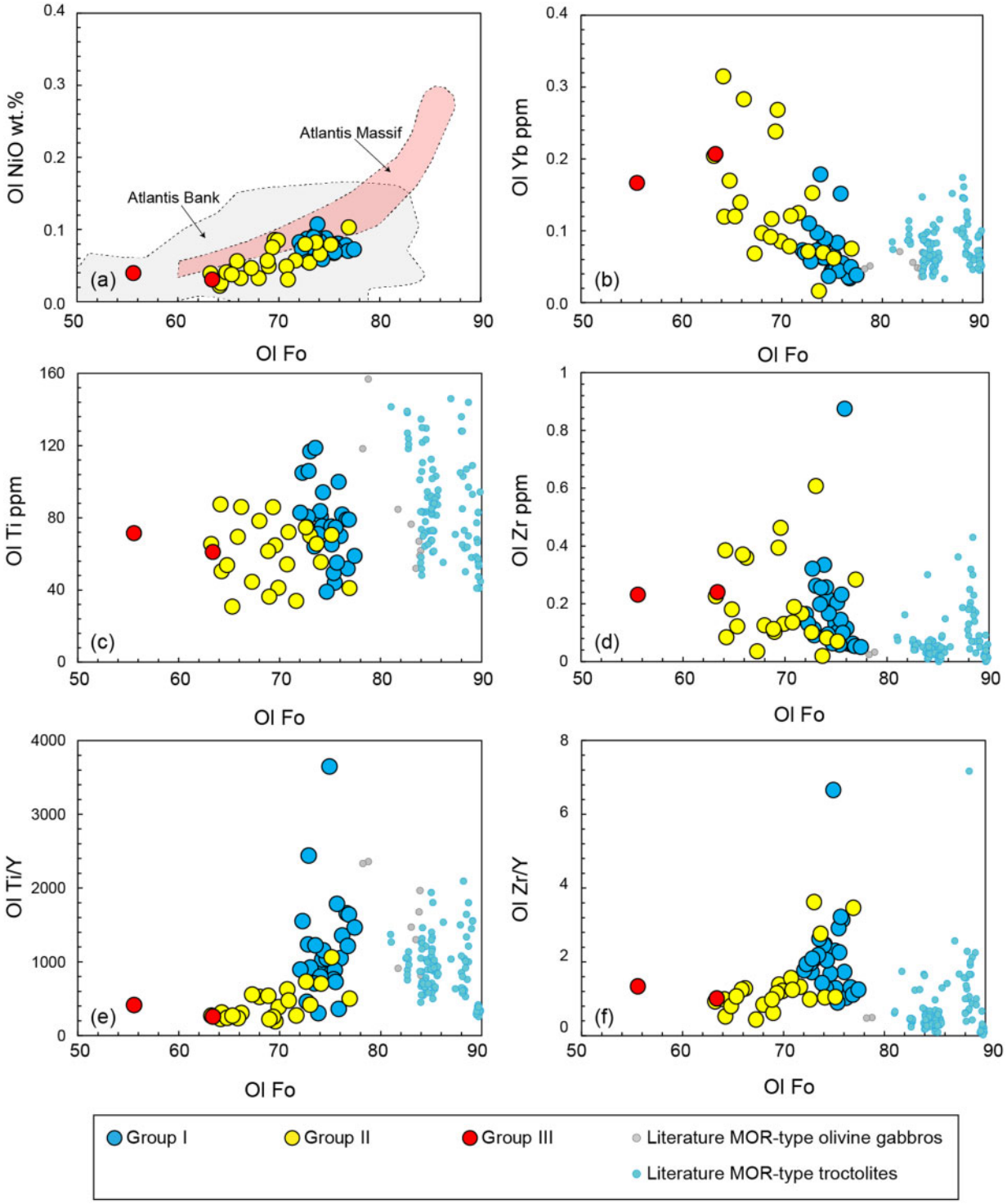

Fig. 9 Olivine (Ol) (a) NiO, (b) Yb contents, (c) Ti, (d) Zr, (e) Ti/Y and (f) Zr/Y ratios plotted against forsterite content (Fo) for Group I, II and III olivine gabbros. Compositional fields of the Atlantis Bank (SW Indian Ridge, SWIR) and Atlantis Massif (Mid-Atlantic Ridge, MAR) are from Dick et al. (2002) and Suhr et al. (2008). Literature data of mid-ocean ridge (MOR) -type olivine gabbros and troctolites are from Basch et al. (2018), Drouin et al. (2009), Ferrando et al. (2018), Lissenberg et al. (2013) and Rampone et al. (2016).

(averaged value of 1318±534), exhibiting the poorly-defined Ti/Y– anorthite content correlations with shallower slopes than those for Group I plagioclase (Fig. 11e). Unlike clinopyroxene, plagioclase Ce–Y correlations for all samples are poorly-defined (R^2=0·06, Fig. 11f). In general, plagioclase rims exhibit higher Ce but slightly lower Y contents than the cores (Fig. 10h, i and Fig. 11f). Accordingly, plagioclase cores have Ce/Y ratio (mean value of 3·5±2·5) lower than the rims (mean value of 7·3±2·9).

Downloaded from https://academic.oup.com/petrology/article/61/9/egaa082/5890488 by Institute of Geology and Geophysics, CAS user on 04 March 2021

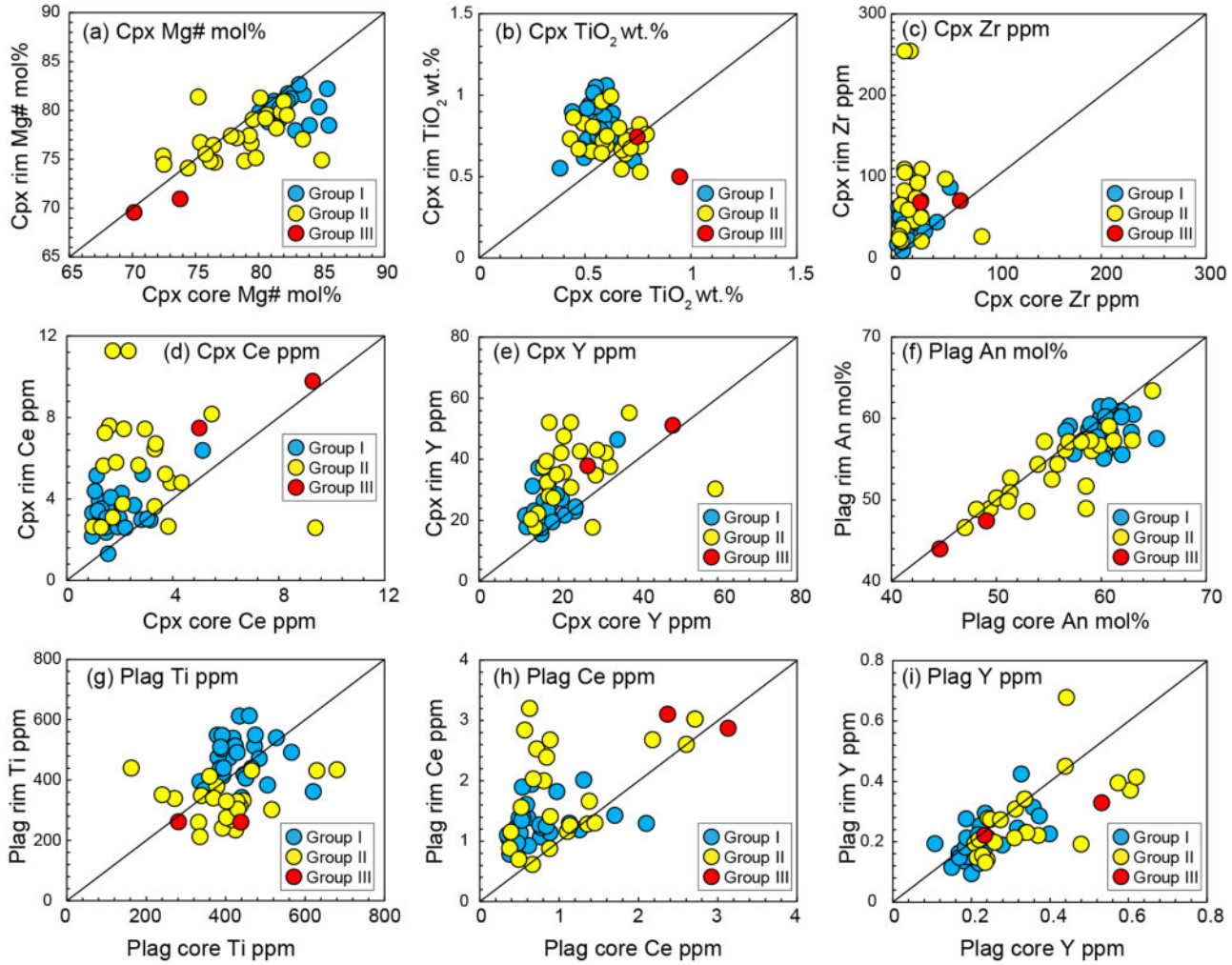

Fig. 10 Core and rim compositions for clinopyroxenes (Cpx, a–e) and plagioclases (Plag, f–i). Black lines show 1:1 proportion of clinopyroxene and plagioclase compositions.

Orthopyroxene

Orthopyroxenes analysed in this study are all fine-grained interstitial grains. Group I orthopyroxene exhibits Mg# varying from 75 to 81 mol %, comparable to Group II (69–81 mol %) but higher than Group III (65–69 mol %). Orthopyroxene Mg# exhibit well-defined correlations with olivine forsterite contents (R^2=0·9, Fig. 7b). Group I orthopyroxene has higher TiO_2 at a given Mg# with respect to Group II and III orthopyroxene (Fig. 12a). Notably, Group II orthopyroxene has TiO_2 contents significantly lower than most orthopyroxene in Hole 735B gabbros (Dick et al., 2002) at a given Mg# (Fig. 12a).

Orthopyroxene trace element patterns exhibit LREE depletion relative to HREE (La_N/Yb_N = 0·001–0·025) and weak to moderate negative Eu anomalies (Fig. 8g, h). Orthopyroxene is depleted in highly incompatible trace elements (from Th to Sr) but exhibit enrichments in HFSE (Fig. 8g, h). There is a prominent decrease in orthopyroxene Ti/Y ratios and Mg# from Group I (mean Ti/Y ratios of 669±211) to Group II (mean Ti/Y ratios of 486±411) and Group III (mean Ti/Y ratios of 316±214) olivine gabbros (Fig. 12b). In comparison, orthopyroxene in Group I olivine gabbros exhibits Zr/Y ratios comparable to Group II (Zr/Y = 0·4–2·1) yet higher than Group III olivine gabbros (Zr/Y = 0·7–1·0) (Fig. 12c).

Whole-rock geochemistry

Group I olivine gabbros have Mg# (=Mg^{2+}/Mg^{2+}+Fe^{2+}_{total},) varying from 75 to 79 mol %, generally higher than Group II (mean Mg# of 73 mol %) and Group III (Mg#=61 mol %). All olivine gabbros are depleted in LREE and HFSE relative to the moderately incompatible trace elements (e.g., HREE). They also exhibit positive Eu, Sr and negative Ti, Zr, Hf anomalies (Fig. 8i, j). There are progressive increases in Ti, Zr, LREE (e.g., Ce) and HREE (e.g., Yb) contents, and decreases in Mg# from Group I to Group III olivine gabbros (Fig. 13a-d). Three groups of olivine gabbros exhibit indistinguishable La/Sm ratios, showing poorly-defined La/Sm–Mg# correlations (Fig. 13e). Group I olivine gabbros have slightly higher Ti/Y ratios than Group II and III, i.e., Ti/Y ratios are 224±30, 205±39 and 203±45 for Group I, II and III, respectively (Fig. 13f).

Downloaded from https://academic.oup.com/petrology/article/61/9/egaa082/5890488 by Institute of Geology and Geophysics, CAS user on 04 March 2021

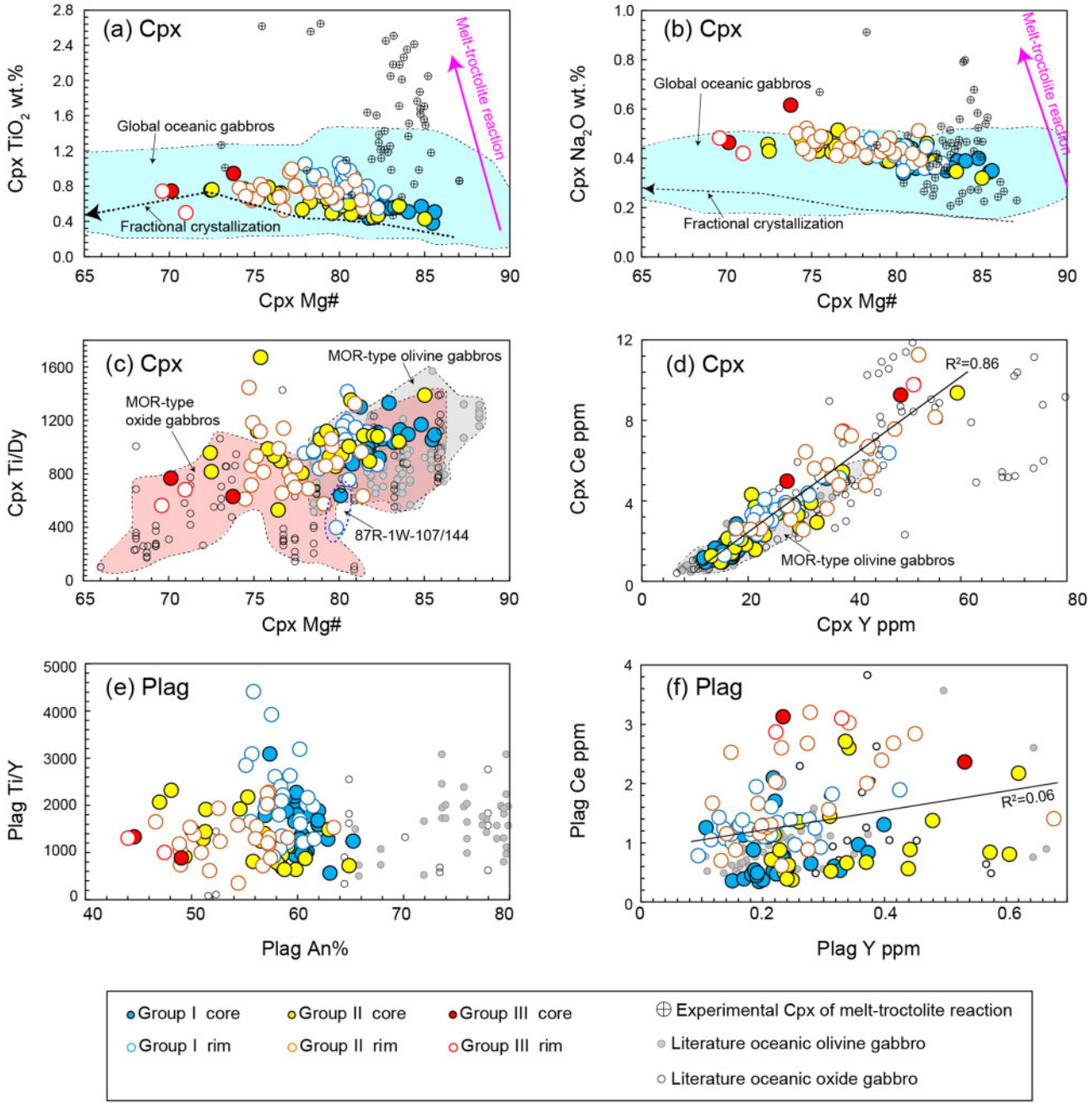

Fig. 11 Clinopyroxene (a) TiO_2, (b) Na_2O and (c) Ti/Dy ratios vs clinopyroxene Mg#, (d) clinopyroxene Ce vs clinopyroxene Y content, (e) plagioclase (Plag) Ti/Y ratios vs anorthite contents, and (f) plagioclase (Plag) Ce vs Y content. Compositional fields of global oceanic gabbros and the clinopyroxene formed by the melt-troctolite reaction experiments are from Yang et al. (2019). The literature data for the oceanic olivine gabbros and oxide gabbros are from: Hess Deep (East Pacific Rise, EPR) (Lissenberg et al., 2013), Atlantis Massif (Mid-Atlantic Ridge, MAR) (Drouin et al., 2009), MARK region (MAR) (Cortesogno et al., 2000), Godzilla Megamullion (Philippine Sea) (Harigane et al., 2019; Sanfilippo et al., 2016).

Chemical stratigraphy

Major element parameters (Mg#, forsterite content and anorthite content) for Group I and II olivine gabbros define three stratigraphic trends with upward decreases in mineral and whole-rock Mg# and plagioclase anorthite contents, with two major discontinuities at 90 and 300 mbsf (Fig. 14a-e). Group III olivine gabbros are too low in mineral and whole-rock Mg# and plagioclase anorthite contents to match the main stratigraphic trends defined by Group I and II olivine gabbros (Fig. 14a-e).

Whole-rock Zr/Y ratios display upward decrease from 809 to 500 mbsf, while no well-defined stratigraphic variations of whole-rock Zr/Y ratios are present above 500 mbsf (Fig. 15a). To assess whether the olivine gabbro phase assemblage is in equilibrium with Atlantis Bank MORB, we used partition coefficients from the literature to calculate equilibrium mineral trace element

Downloaded from https://academic.oup.com/petrology/article/61/9/egaa082/5890488 by Institute of Geology and Geophysics, CAS user on 04 March 2021

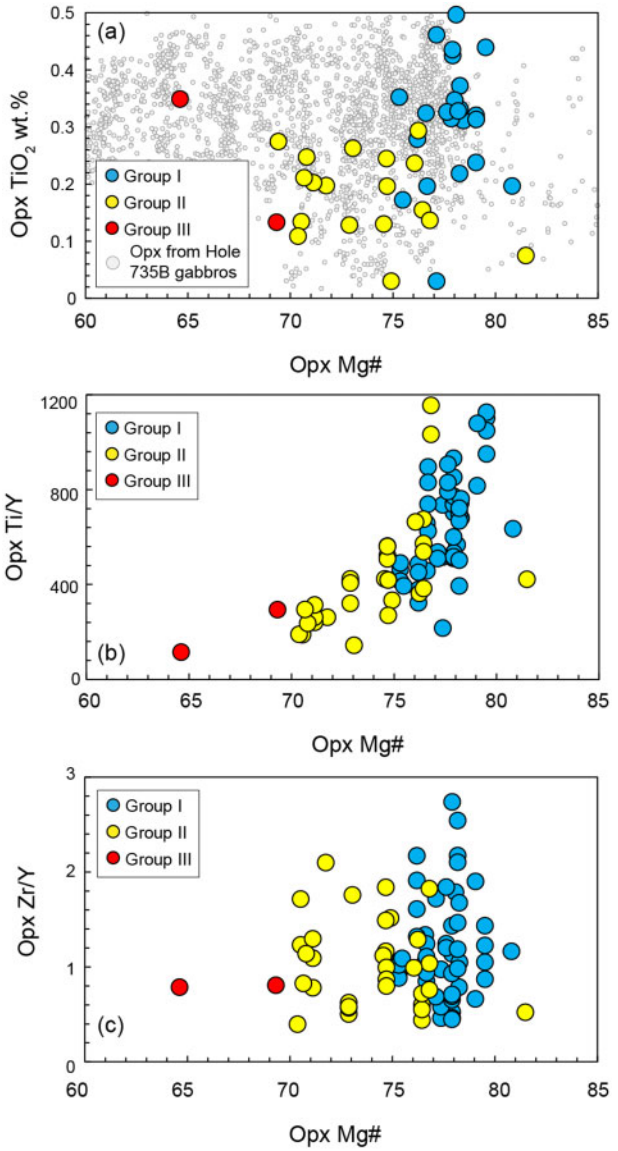

Fig. 12 (a) Orthopyroxene TiO_2 content, (b) Ti/Y ratios, and (c) Zr/Y ratios vs orthopyroxene Mg#. Orthopyroxene data for Hole 735B gabbros (Atlantis Bank, SWIR) are from Dick et al. (2002).

abundances for each phase (See Fig. 15 for calculation details). Zr/Y ratios in clinopyroxene cores are low and uniform throughout this hole, with values comparable to the equilibrium clinopyroxene of the Atlantis Bank MORB (Fig. 15b); on the other hand, Zr/Y ratios in clinopyroxene rim are generally higher than the equilibrium clinopyroxene (Fig. 15b). Plagioclase cores display low and uniform Ce/Y ratios in apparent equilibrium with the Atlantis Bank MORB (Fig. 15c), whereas plagioclase rim Ce/Y ratios are elevated relative to cores as well as the equilibrium plagioclase of the Atlantis Bank MORB (Fig. 15c).

Most olivine from 589–809 mbsf interval (Group I) display higher Zr/Y ratios than calculated equilibrium olivine. In comparison, olivine in 0–589 mbsf interval (Group II) and local shear zones (Group III) generally exhibit low and uniform Zr/Y ratios, with values slightly higher than the equilibrium olivine (Fig. 15d). Orthopyroxene exhibits comparable Zr/Y ratios throughout this hole, with values generally higher than the calculated equilibrium orthopyroxene (Fig. 15e).

Clinopyroxene-plagioclase REE equilibration temperatures

Crystallization temperatures for clinopyroxene and plagioclase were obtained by the REE-in-plagioclase–clinopyroxene geothermometer (Sun & Liang, 2017). In general, except for Eu, both LREE and HREE can define a linear trend of (B/100) versus (lnD-A) plot for both mineral rims and cores, as, for instance, shown by the sample 65R-2W-74/81 (Fig. 16a). This indicates that both LREE and HREE between clinopyroxene and plagioclase have reached equilibrium. Thus, clinopyroxene-plagioclase REE equilibration temperatures provide useful estimates of the crystallization or reequilibration temperatures for clinopyroxene and plagioclase core and rim pairs. The upper limits of REE equilibration temperatures for Group I and II olivine gabbros from different depths throughout this hole are comparable, varying from 1,160 to 1,150°C (Fig. 16b). Group I olivine gabbros gave REE equilibration temperatures ranging from 1,160°C down to ~1,050°C. By contrast, Group II olivine gabbros have a larger range from 1,160° down to 1,010°C. Similarly, the mean clinopyroxene-plagioclase rim REE equilibration temperatures for Group I are higher (1080±24°C) than for Group II (1058±45°C).

Geospeedometry

Mg-REE-coupled geospeedometer for clinopyroxene and plagioclase (Sun & Lissenberg, 2018) and Ca-in-olivine geospeedometer (Coogan et al., 2007) have been applied to calculate the cooling rate, with results plotted in Fig. S2 and values given in Table S8. The cooling rates given by the two methods are comparable, varying from 10^{-3} to 10^{-2} °C/yr (Fig. S2). The mean cooling rates of Group I olivine gabbro ($10^{-2.4\pm0.4}$ °C/yr) appear to be slightly lower than those of Group II ($10^{-2.0\pm0.4}$ °C/yr) and III ($10^{-1.9\pm0.4}$ °C/yr), however we note that all three groups are within calculated uncertainties.

DISCUSSION

Episodic intrusion and parental melt compositions

Magmatic accretion at slow- and ultraslow-spreading ridges is characterized by episodic intrusions (Bloomer et al., 1991; Dick, 1991; Sinton & Detrick, 1992). At Atlantis Bank gabbroic massif, episodic intrusions are seen in three upward magma differentiation trends, i.e., the progressive upward decreases in mineral and whole-rock Mg# and plagioclase anorthite contents (Fig. 14a–e) in Hole U1473A, corresponding to three intrusive cycles at 0–90 mbsf, 90–300 mbsf and 300–809

Downloaded from https://academic.oup.com/petrology/article/61/9/egaa082/5890488 by Institute of Geology and Geophysics, CAS user on 04 March 2021

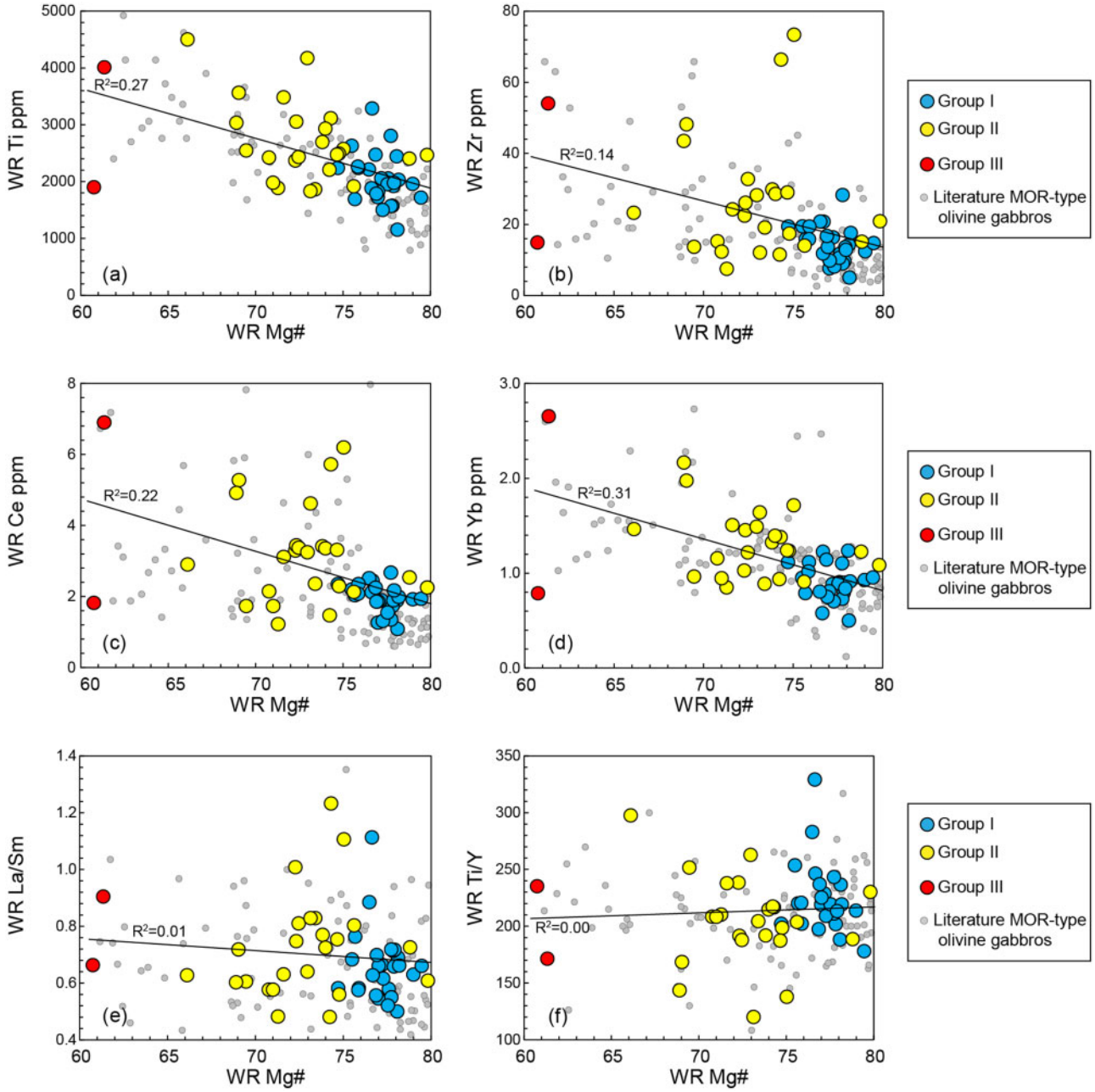

Fig. 13 Whole-rock (WR) (a) Ti, (b) Zr, (c) Ce, (d) Yb, (e)La/Sm ratios, and (f) Ti/Y ratios plotted against Mg#. Literature olivine gabbro data are from: Atlantis Bank (Coogan et al., 2001a) and the Atlantis Massif (Godard et al., 2009).

mbsf. There are abundant evidences supporting the compaction of cumulate piles in the less deformed samples, i.e., plagioclase grains showing deformation twins (Fig. 4e) and local blended plagioclase grains (Fig. 4f) (Holness et al., 2017; Meurer and Boudreau, 1998). Thus, we ascribe the three upward magma differentiation trends in Hole U1473A to the compaction-driven melt migration up through a cumulate pile consisting of early crystallized plagioclase, olivine, and clinopyroxene (Dick et al., 2019b). Melt migration in this stage was limited by thermal boundaries and with variable internal porosity of the crystal mush, resulting in the formation of a chemical discontinuity (Dick et al., 2019b).

Applying the Fe–Mg distribution coefficients for clinopyroxene from equation 14 in Bédard (2010), we calculated the Mg# of melts in equilibrium with clinopyroxene in olivine gabbros. Equilibrium melts of Group I clinopyroxene have Mg# ranging from 43 to 58, which is less evolved with respect to those of Group II (Mg#=33–56) and III clinopyroxene (Mg#=27–37). In general, the equilibrium melts of all olivine gabbros are too evolved to match Atlantis Bank basalts (Mg#=55–73 (Coogan et al., 2004)).

The REE compositions of melts in equilibrium with the olivine gabbros were calculated from clinopyroxene REE compositions (Fig. 17), using clinopyroxene-melt

Downloaded from https://academic.oup.com/petrology/article/61/9/egaa082/5890488 by Institute of Geology and Geophysics, CAS user on 04 March 2021

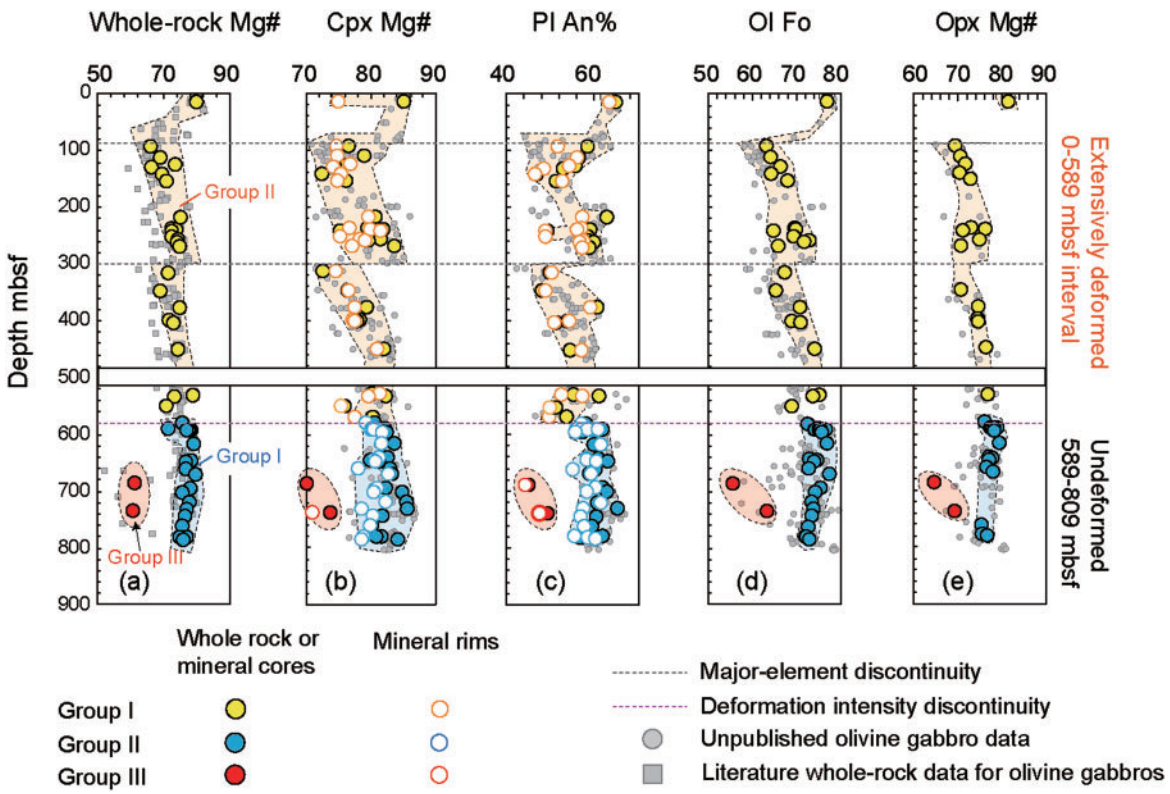

Fig. 14 Down-hole mineral composition plots for Hole U1473A (a) whole-rock Mg#, (b) clinopyroxene (Cpx) Mg#, (c) plagioclase anorthite content, (d) olivine forsterite content (Ol Fo), (e) orthopyroxene (Opx) film Mg#. Black dashed lines represent the two chemical discontinuities at 90 and 300 mbsf. Pink dashed line is the deformation intensity discontinuity at ~589 mbsf. Literature whole-rock data for olivine gabbros are from Ciazela (2018) and MacLeod et al. (2017). Our unpublished mineral major element data for olivine gabbros are given in (b–e) for comparison.

REE partition coefficients calculated based on lattice strain model of Sun and Liang (2012). The temperatures for the equilibrium melt calculations are based on REE-in-plagioclase-clinopyroxene thermometer from Sun and Liang (2017). The pressure and water content are set to be 2 kbar and 0·2 wt %, respectively. We plot the REE patterns of the most depleted equilibrium melts in each group to represent their parental melt composition (Fig. 17a). For comparisons, we computed the parental melt REE composition based on clinopyroxene-melt partition coefficients from Hart and Dunn (1993). Prominent discrepancies in the parental melt REE compositions between the two suites of partition coefficients are present (Fig. S3), which indicates the significant effects of clinopyroxene major element composition and temperature on clinopyroxene-melt REE partitioning (Sun and Liang, 2012).

The calculated REE patterns and abundances of the most depleted melts for Group I and Group II olivine gabbros share similarities with the most depleted end member of the contemporaneous (10–13 Ma) Atlantis Bank MORB recovered from nearby rift mountains (Fig. 17a). The most depleted computed melts for Group I and II olivine gabbros exhibit nearly identical REE abundances and patterns, without prominent Eu anomalies (Eu/Eu*=0·91–0·95) (Fig. 17a). This similarity suggests that both Group I and II olivine gabbros might start in equilibrium with a relatively depleted MORB magma. The most depleted computed melts of Group III olivine gabbros exhibit prominent LREE enrichments (i.e. La_N/Yb_N =2·5), distinct from those of Group I and II olivine gabbros (i.e. La_N/Yb_N =0·5–0·6) and the contemporaneous basalts (i.e. La_N/Yb_N =0·6–1·3) (Fig. 17a). Thus, Group III olivine gabbros were derived from a LREE-enriched melt.

Nevertheless, the most enriched equilibrium melts of the three groups are nearly identical in the REE patterns and abundances, i.e., elevated LREE/HREE ratios (La_N/Yb_N =0·8–1·2) and prominent negative Eu anomalies (Eu/Eu*=0·3–0·.5) (Fig. 17b). Additionally, these melts possess higher REE abundances than the contemporaneous (10–13 Ma) Atlantis Bank MORB, implying the interstitial melts in these gabbros experienced higher degrees of differentiation than the erupted melts.

Petrological evidences for multi-stage melt-rock reaction

Textures indicative of oxide-undersaturated melt-rock reaction in olivine gabbros from less deformed interval (Group I)

Fractional crystallization of MORB along a typical liquid line of descent leads to saturation of oxides only after significant crystallization (e.g. ~70% crystallization of

Downloaded from https://academic.oup.com/petrology/article/61/9/egaa082/5890488 by Institute of Geology and Geophysics, CAS user on 04 March 2021

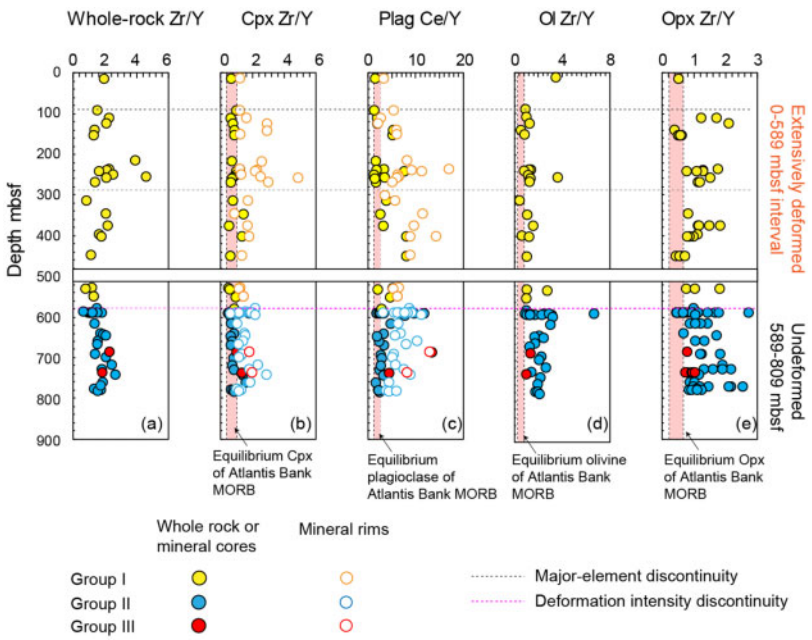

Fig. 15 Down-hole mineral composition plots for (a) whole-rock Zr/Y ratio, (b) clinopyroxene (Cpx) rim Zr/Y ratio, (c) plagioclase (Plag) rim Ce/Y ratio, (d) olivine (Ol) core Zr/Y ratio, (e) orthopyroxene (Opx) film Zr/Y ratio. Equilibrium minerals of the Atlantis Bank MORB are calculated using basalt data from Coogan et al. (2004). The values and sources of the partition coefficients for clinopyroxene, orthopyroxene and olivine are given in Table S9. The plagioclase-melt partition coefficients for Ce and Y are calculated, assuming the temperatures of 1100°C, pressures of 2 kbar, and following the model by Sun et al. (2017). Black dashed lines represent the two chemical discontinuities at 90 and 300 mbsf. Pink dashed line is the deformation intensity discontinuity at ~589 mbsf.

primitive Southwest Indian Ridge MORB (Chen et al., 2019)). Textural disequilibrium among minerals are ubiquitous in Group I olivine gabbros, likely due to reaction with modestly evolved melts (i.e. oxide-undersaturated melts). For instance, embayed plagioclase is juxtaposed against a large clinopyroxene oikocryst with resorbed to planar sharp contacts (Fig. 4a). Further, olivine oikocrysts exhibit irregular to straight contacts against plagioclases (Fig. 4b). Corroded olivine grains with resorbed or irregular shapes are enclosed by clinopyroxene and plagioclase (Fig. 4c). The occurrence of clinopyroxene oikocrysts enclosing either resorbed plagioclase (Fig. 4a) or the relict of corroded olivine (Fig. 4c) indicates a reaction in which dissolution of olivine and plagioclase occurred contemporaneously with the precipitation of clinopyroxene. Recent studies on the clinopyroxene oikocrysts in oceanic cumulates suggest dissolution–reprecipitation processes triggered by the infiltration of primitive melts into gabbros (e.g., Leuthold et al., 2018; Lissenberg and Dick, 2008). In addition, olivine can occur as oikocrysts with interstitial extensions filling the boundaries between plagioclase chadacrysts (see the red arrows in Fig. 4b), which implies precipitation of olivine. Plagioclase often encloses resorbed small olivine grains (e.g., Fig. 4c), which implies precipitation of plagioclase during dissolution of olivine. Taken as a whole, we suggest the textures of Group I olivine gabbros are compatible with dissolution and reprecipitation of olivine, plagioclase, and clinopyroxene. As these textures are not associated with Fe–Ti oxide (i.e. ilmenite), we suggest the dissolution and reprecipitation processes were likely induced by the infiltration of an oxide-undersaturated melt into olivine gabbros.

Textures indicative of multi-stage melt-rock reaction in olivine gabbros from shear zones (Group II and III)

Textural features of Group II and III olivine gabbros imply a more complex history than Group I olivine gabbros. For instance, the presence of poikilitic, optically uniform clinopyroxenes enclosing plagioclase chadacrysts with straight contacts (Fig. 5a) and large clinopyroxene grains enclosing corroded olivine with irregular contacts in Group II olivine gabbros (Fig. 5b) suggest a multifaceted provenance. In Group III olivine gabbros (83R-6W-9/23), there are small, resorbed plagioclase grains embayed by large olivine crystals (Fig. 5g). These microtextural observations in Group II and III olivine gabbros are compatible with the features of Group I olivine gabbros, which as we have shown are not directly associated with the precipitation of ilmenite and brown amphibole. We suggest these textures, in the absence of amphibole and ilmenite, are related to a reaction with oxide-undersaturated melts.

In addition, there are abundant textures indicating the oxide-saturated melt infiltration in Group II and III olivine gabbros. Textures show corroded olivine (Fig. 5d, h), clinopyroxene and plagioclase (Fig. 5d, e) rimmed by ilmenite with irregular or lobate contacts in Group II olivine gabbros. The undeformed aggregates of ilmenite and brown amphibole often fill the

Downloaded from https://academic.oup.com/petrology/article/61/9/egaa082/5890488 by Institute of Geology and Geophysics, CAS user on 04 March 2021

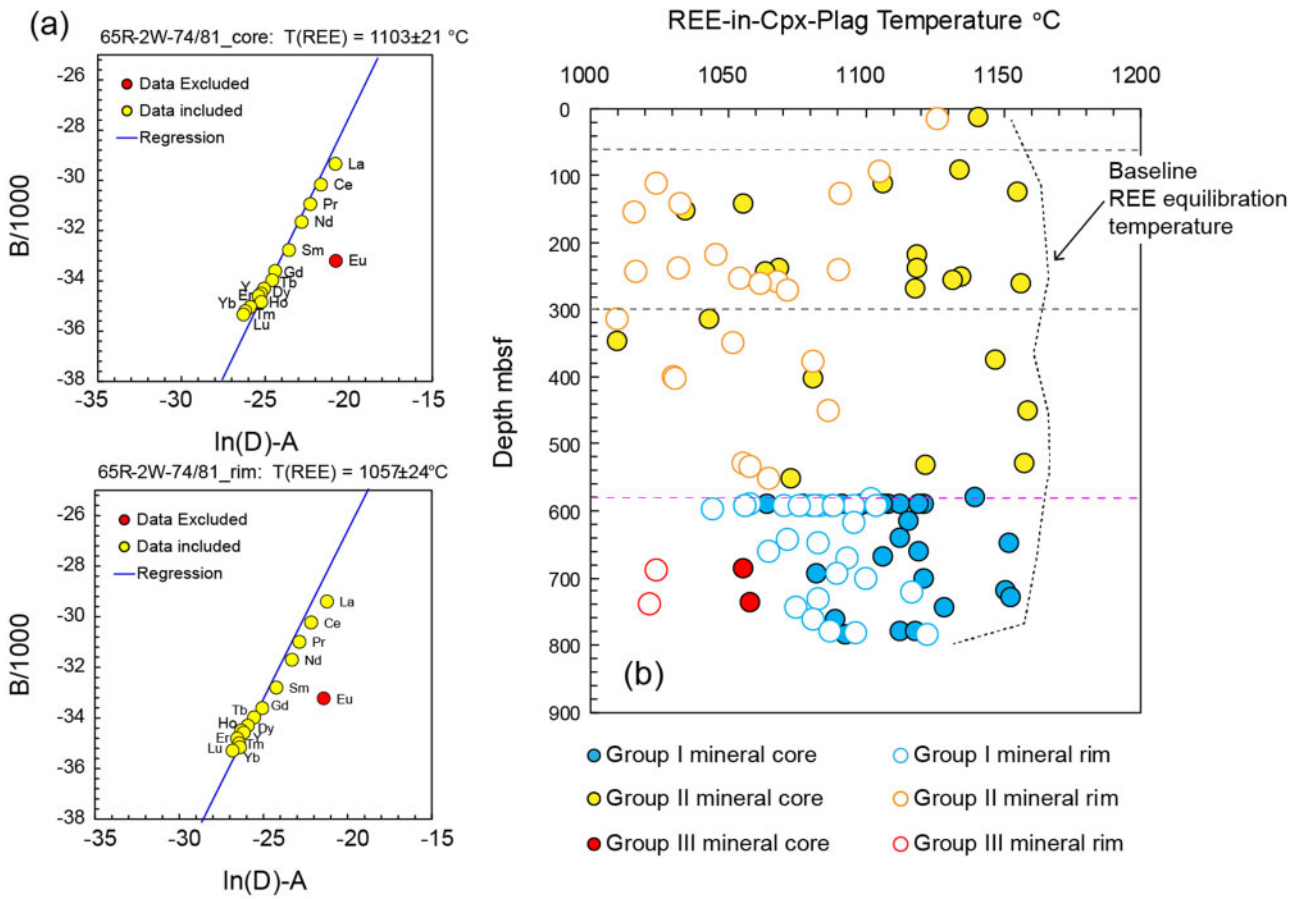

Fig. 16 Clinopyroxene-plagioclase REE equilibration temperatures. (a) The representative (B/100) vs (ln(D)-A) plot testing whether clinopyroxene and plagioclase have reached the LREE and HREE equilibrations; (b) the stratigraphic variations of clinopyroxene-plagioclase REE equilibration temperatures. The black dashed line labels the upper limit of REE equilibration temperatures of samples from different depths throughout this hole. The grey dashed horizontal lines label the major element discontinuities at ~90 and 300 mbsf, respectively. The pink dashed horizontal line labels the ~589 mbsf deformation intensity discontinuity.

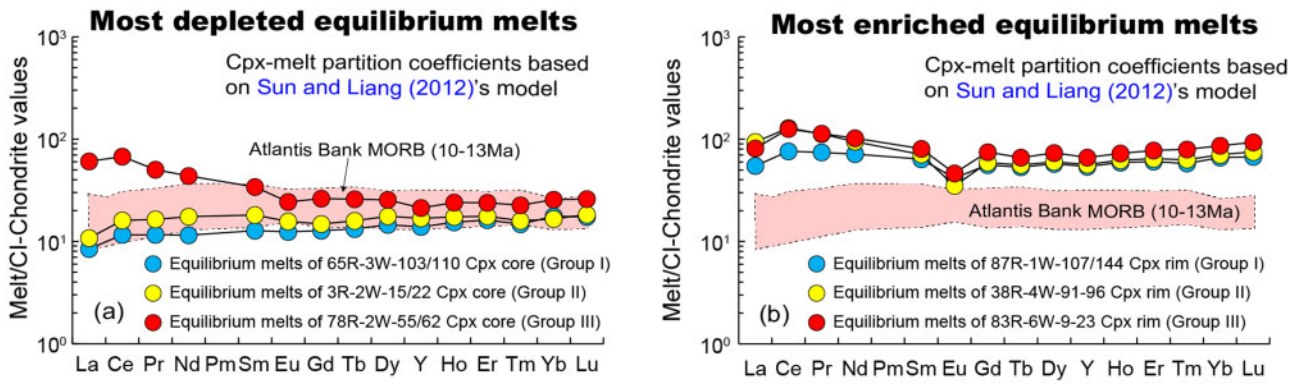

Fig. 17 REE patterns of (a) most depleted and (b) most enriched equilibrium melts based on clinopyroxene (Cpx). The Atlantis Bank MORB (10–13 Ma) data from Coogan et al. (2004) are shown for comparisons. Partition coefficients are calculated, following the model by Sun and Liang (2012) and assuming the temperature of 1100°C and pressure of 2 kbar.

boundaries between the neoblastic plagioclase and corroded clinopyroxene (Fig. 5f), implying the infiltration of water-rich and oxide-saturated melts in Group II olivine gabbros. Similar textures related to dissolution/precipitation processes are also present in Group III olivine gabbros (Fig. 5h). In sample 78R-2W-55/62 (Group III), the dissolution of olivines by Fe–Ti oxide-saturated melts is preserved as highly corroded olivine grain embayed against the complex aggregate of clinopyroxene, orthopyroxene and ilmenite (Fig. 5i). These features indicate the precipitation of ilmenite, orthopyroxene and brown amphibole at the expense of olivine, plagioclase and clinopyroxene. As the ilmenite occurs as a relatively late-stage, low-temperature

Downloaded from https://academic.oup.com/petrology/article/61/9/egaa082/5890488 by Institute of Geology and Geophysics, CAS user on 04 March 2021

differentiate, i.e., <1100°C (e.g., Botcharnikov et al., 2008; Koepke et al., 2018), we suggest that the precipitation of ilmenite is a result of late-stage melt-rock reaction.

In general, most Group II and III olivine gabbros have experienced various degree of ductile deformation which prominently modified the initial textures. Only in the coarse-grained and less-deformed samples, the textures for both stages of melt-rock reaction are present (e.g., Fig. 18). Clinopyroxene in sample 28R-4W-129/136 occurs as oikocrysts with irregular contact against olivine and plagioclase (Fig. 18a, b). The rims of these clinopyroxene oikocrysts and plagioclase exhibit lobate contacts against ilmenite and brown amphibole (Fig. 18c, d). In sample 25R-1W-93/100, clinopyroxene occurs as oikocryst enclosing resorbed plagioclase chadacrysts (Fig. 18e, f). Meanwhile, this clinopyroxene oikocryst shows lobate contacts against ilmenite and brown amphibole (Fig. 18g, h). Similar clinopyroxene oikocrysts were reported in Kane Megamullion (MAR) cumulates (i.e. Type I and II oikocrysts, see Lissenberg and Dick (2008)), and explained by a reaction with relatively primitive melts. In the two thin sections, the rims of clinopyroxene oikocrysts were corroded and partially replaced by ilmenites and brown amphiboles (Fig. 18c, d, g, h), which is compatible with the late reaction with oxide-saturated melts. These features imply that the olivine gabbros in shear zones (i.e. Group II and III) experienced multi-stage melt-rock reactions, from early-stage reaction with oxide-undersaturated melts to late-stage reaction with oxide-saturated melts. In comparison, olivine gabbros from less deformed intervals (Group I) merely record the early-stage reaction with oxide-undersaturated melts.

Trapped melt fractions (TMF) and whole-rock Ti/REE fractionations

Whole-rock compositions of oceanic cumulate are commonly envisaged to be the compositions of the cumulus minerals plus the interstitial melts trapped between them. The whole-rock incompatible trace elements of the gabbros can be used to calculate the trapped melt fractions (TMF) (Bédard, 1994; Coogan et al., 2001a; Meyer et al., 1989; Natland et al., 1991). Following the methods described in Coogan et al. (2001a), we calculated the TMF of Hole U1473A olivine gabbros. The compositions of the melts in equilibrium with the gabbros were calculated from the regressions of basalt Mg# (assuming a molecular Fe^{2+}/total Fe of 0·86) and incompatible trace elements using the 10–13 Ma basalt data from Coogan et al. (2004). Then, the fractions of interstitial melts can be calculated using the mass balance equation from Bédard (1994) (equation 2). The partition coefficients for Ti, Zr and REE are given in Table S9. The partition coefficients for Nb and P are from Coogan et al. (2001a).

In Fig. 19a, we plot the mean TMF versus the bulk partition coefficients for different groups of olivine gabbros. In general, there is a progressive increase in TMF from Group I to Group II and III for most elements (except for P). In addition, the mean TMF for each group increase with the increasing compatibility of selected elements, with values of 3–6% for Nb but 8–18% for Y (Fig. 19a). This is because the more incompatible trace elements will tend to be taken into interstitial melts and be removed from the crystal mush by porous melt flow (Coogan et al., 2001a). Thus, we use the TMF calculated from the highly incompatible trace element (i.e. Nb) to represent the residual melt fractions of our samples, yielding the mean values of 3%, 6% and 6% for Group I, II, and III, respectively. These results are consistent with the previous analysis on the Hole 735B olivine gabbros (Natland et al., 1991). The progressive increase in TMF from Group I to Group II and III is compatible with the increase in the intercumulus phases (i.e. brown amphibole, Fe–Ti oxides, Fig. S1b).

Group II and III olivine gabbros exhibit negative Ti/Y–La/Sm correlations, which contrasts with the Group I olivine gabbros (Fig. 19b). We preclude the accumulation of clinopyroxene, olivine, and plagioclase as the origin of the whole-rock Ti/Y fractionation, as these olivine gabbros are nearly identical in cumulus mineral modes (Fig. 19b). The accumulation of ilmenite and magnetite is also unlikely to produce the negative Ti/Y–La/Sm correlations, as they are represented by extremely high Ti/Y ratios ($>10^5$) and very low REE contents (e.g. She et al. (2015)). Noteworthily, Group II and III olivine gabbros exhibit negative correlations between Ti/Y ratios and TMF estimated based on whole-rock Nb contents (Fig. 19c), which is compatible with the entrapment of melts that have experienced prominent Fe–Ti oxide fractionation. Thus, the entrapments of oxide-saturated melts might prominently affect the Ti/REE fractionations of the olivine gabbros from shear zones (Group II and III).

Mineral HFSE/REE fractionations in olivine gabbros from less deformed zones (Group I): Reaction with oxide-undersaturated melts

Minerals in Group I olivine gabbros are represented by their significant HFSE/REE fractionation, which is summarized as follows:

1. Group I clinopyroxene has Zr/Nd ratios varying from 4–12. By contrast, except for one sample (87R-1W-107/144), the Ti/Dy ratios in Group I clinopyroxene are roughly uniform, with values of 1042±120 (Fig. 11c).
2. Group I plagioclase exhibits Ti/Y ratios increasing from 864–4776 with the decreasing anorthite contents (Fig. 11e).
3. Group I olivine shows high and variable Ti/Y and Zr/Y ratios, with values ranging from 302– 3646 and from 0·9–6·7, respectively (Fig. 9e, f).
4. Group I orthopyroxene has high and variable Ti/Y and Zr/Y ratios, with values varying from 217 –1127 and 0·4–2·7 (Fig. 12b, c).

Downloaded from https://academic.oup.com/petrology/article/61/9/egaa082/5890488 by Institute of Geology and Geophysics, CAS user on 04 March 2021

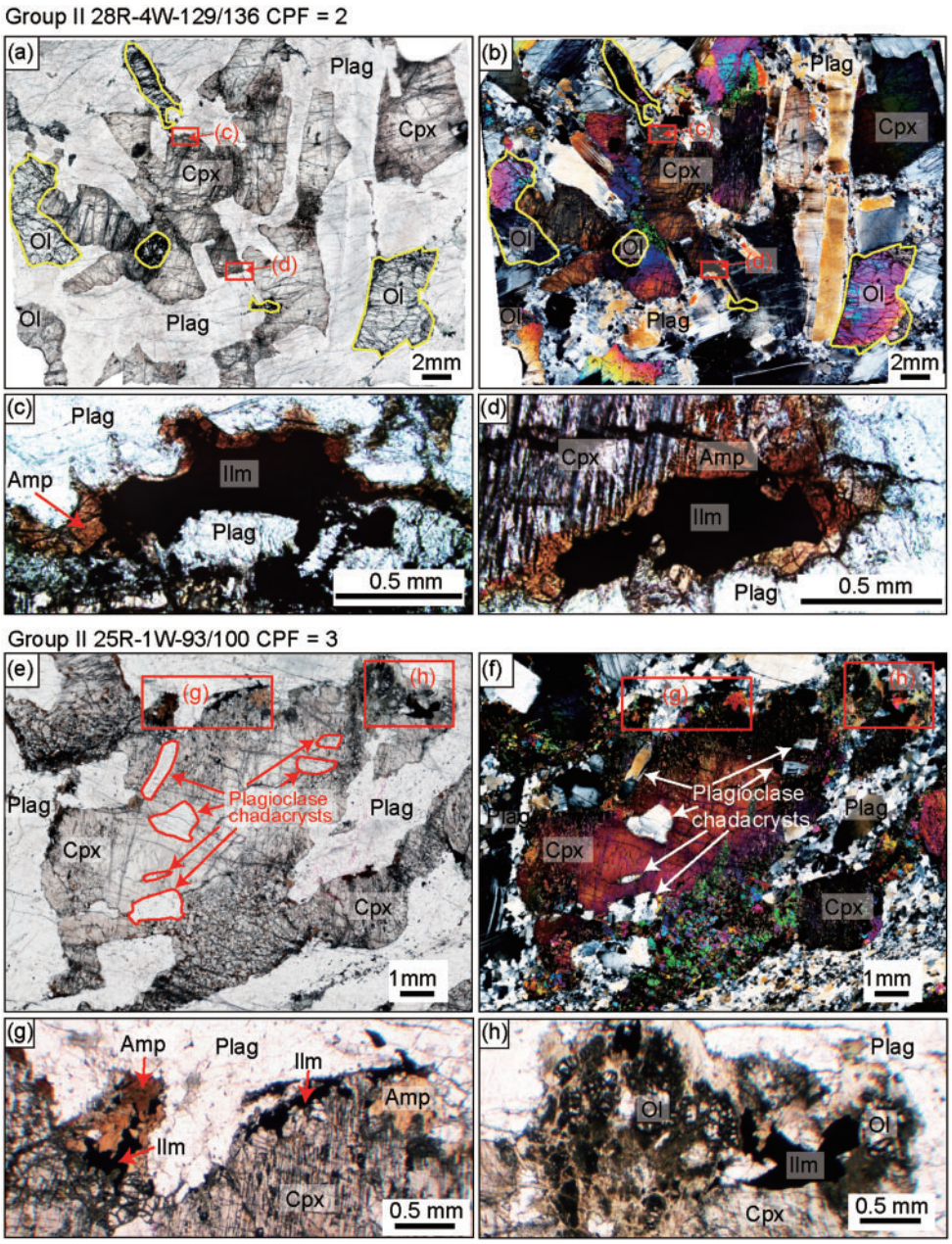

Fig. 18 Textures showing the multi-stage evolution of Group II olivine gabbros. (a–b) clinopyroxene oikocrysts with irregular contacts against more euhedral olivine and plagioclase and (c–d) corroded clinopyroxene and plagioclase with lobate contacts against ilmenite and brown amphibole in sample 28R-4W-129/136; (e–f) clinopyroxene oikocrysts enclosing small resorbed plagioclase chadacrysts and (g–h) corroded clinopyroxene rims and plagioclases partially replaced by ilmenites and brown amphibole in sample 25R-1W-93/100. In (a) and (b), the boundaries between olivine and other minerals are labeled in yellow curves. Abbreviations are as follows: Ol, olivine; Plag, plagioclase; Cpx, clinopyroxene; Opx, orthopyroxene; Ilm, ilmenite; Amp, brown amphibole.

Previous studies have shown that the HFSE/REE fractionation in minerals from oceanic gabbros are compatible with melt-rock reaction induced by the porous melt migration (e.g., Coogan et al., 2000; Gao et al., 2007). However, the prominent HFSE/REE fractionation in minerals might also be ascribed to equilibrium crystallization and *in-situ* crystallization (e.g., Borghini and Rampone, 2007). In this section, we performed series of geochemical modelling to assess the process controlling the trace element fractionation and to reproduce the mineral (clinopyroxene, olivine and orthopyroxene) HFSE/REE fractionations in Group I olivine gabbros. As the cooling processes of oceanic gabbros can give rise to prominent REE fractionations in plagioclases (e.g., Coogan and O'Hara, 2015), the modelling of HFSE/REE fractionations in plagioclase was not performed here.

Geochemical modelling

Assimilation-Fractional-Crystallization (AFC) equation (DePaolo, 1981) was applied for the melt-rock reaction

Downloaded from https://academic.oup.com/petrology/article/61/9/egaa082/5890488 by Institute of Geology and Geophysics, CAS user on 04 March 2021

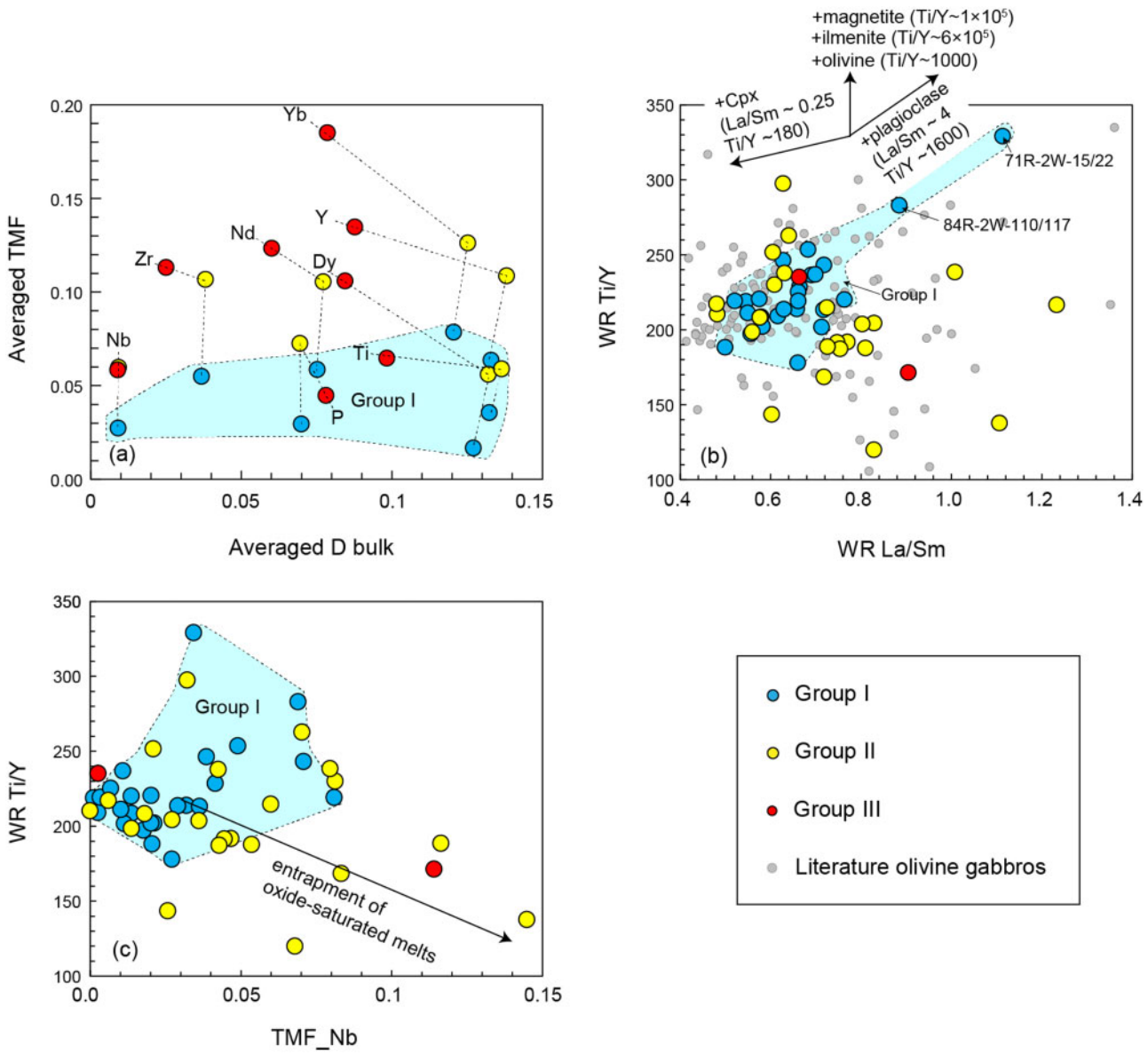

Fig. 19 (a) Estimations of trapped melt fractions (TMF) of Hole U1473A olivine gabbros; (b) whole-rock Ti/Y ratios plotted against whole-rock La/Sm ratios; and (c) trapped melt fraction (TMF) calculated from whole-rock Nb contents. See text for details of TMF calculations. The Ti/Y ratios of ilmenite and magnetite are from the data of Ermeishan layered intrusions (She et al., 2015). Literature olivine gabbro data are from: Atlantis Bank (Coogan et al., 2001a) and Atlantis Massif (Godard et al., 2009).

modelling. The partition coefficients for the geochemical modelling are given in Table S9. The REE partition coefficients for olivine and plagioclase and Ti, Zr, and REE partition coefficients for orthopyroxene are calculated based on the models by the published models (Sun et al., 2017; Sun and Liang, 2013a, b; Yao et al., 2012), using the corresponding mineral compositions for sample 81R-5W-63/70 and assuming the temperature of 1100°C, pressure of 2 kbar, water content of 0·2 wt %. To test the validity of the selected partition coefficients, we calculated the HFSE (Zr, Ti), REE (Nd, Dy, Yb) and Y partitioning among different minerals in Hole U1473A olivine gabbros. As shown in Fig. S4, the intermineral HFSE and REE partitioning for the olivine gabbros are roughly compatible with the selected partition coefficients, indicating that these partition coefficients are valid in geochemical modelling.

Most olivine gabbros exhibit equigranular textures, where clinopyroxene, plagioclase and olivine occur as cumulus phases, e.g., Fig. 3. Orthopyroxene, Fe–Ti oxide and brown amphibole represent the intercumulus phases in these samples. These features are not compatible with the reaction between melts and troctolites where the clinopyroxene should occur as an intercumulus phase (Yang et al., 2019). This inference is also supported by clinopyroxene TiO_2–Mg# and Na_2O–Mg# correlations for the olivine gabbros, which generally follow a low-pressure fractional crystallization trend (Fig. 11a, b). Therefore, we consider the reaction of olivine gabbros with migrating melts in the modelling.

Downloaded from https://academic.oup.com/petrology/article/61/9/egaa082/5890488 by Institute of Geology and Geophysics, CAS user on 04 March 2021

As discussed above, textural observations indicate Group I olivine gabbros experienced the reaction with oxide-undersaturated melts, thus, ilmenite fractionation was not considered here. In oceanic gabbros, melts may become saturated in amphibole at near-solidus conditions (i.e. 800–950°C, e.g., Coogan et al., 2001b; Gillis and Meyer, 2001; Koepke et al., 2018). However, the clinopyroxene-plagioclase REE equilibration temperatures for Hole U1473A olivine gabbros generally exceed 1020°C (Fig. 16b). Thus, we do not consider the fractionation of brown amphiboles in this modelling. By contrast, experimental studies have shown that orthopyroxene can be stable at relatively high temperatures (e.g., ~1100 °C at 2kbar (Feig et al., 2006)) in the MORB system. Moreover, melt-rock reaction processes can stabilize orthopyroxene at higher temperatures than simple fractional crystallization (e.g., Coogan et al., 2002; Koepke et al., 2018). Thus, we consider small amounts of orthopyroxene fractionation in the modellings. Here, we consider the melt-rock reaction as below:

Oxide-undersaturated melt-rock reaction (AFC1): olivine1 + plagioclase1 + clinopyroxene1 + melt1 = olivine2 + plagioclase2 + clinopyroxene2 + orthopyroxene + melt2.

Based on the mineral modal proportions of our samples, we consider the olivine, plagioclase and clinopyroxene proportions of 1·5:5:3·5 and 0·6:5·6:3·8 for assimilation and crystallization, respectively. As orthopyroxene is minor phase in most samples, we consider 1% orthopyroxene fractionation for all models. The initial melt compositions are set to be in equilibrium with the most magnesium-rich clinopyroxene (sample 81R-5W-63/70). The compositions of the most magnesium-rich clinopyroxene (sample 81R-5W-63/70) are used to represent the assimilated clinopyroxene. The assimilated olivine and plagioclase compositions are set to be in equilibrium with the assimilated clinopyroxene.

Additionally, we modelled the equilibrium crystallization (EC1), *in-situ* crystallization (*in-situ* FC1) and fractional crystallization (FC1) to assess their role in the mineral HFSE/REE fractionations in Group I olivine gabbros. The initial melt compositions and fractionated mineral modal proportions are the same as AFC modelling. For the *in-situ* crystallization modelling, we applied the method described in Borghini and Rampone (2007). We consider four steps of equilibrium crystallization, where 20%, 40%, 16% and 14·4% of the total trapped melts were consumed in each step, respectively. The parameters of geochemical modelling are given in Table S9. The results of these geochemical modellings are used to interpret the HFSE/REE fractionations in clinopyroxene, olivine and orthopyroxene.

Mineral HFSE/REE fractionations in olivine gabbros from less deformed zones (Group I) controlled by oxide-undersaturated melt-rock reaction

As opposed to clinopyroxene and orthopyroxene, olivine is a fast-diffusing mineral with respect to HFSE and REE (Spandler et al., 2007; Spandler and O'Neill, 2010). Thus, sub-solidus diffusion may influence the HFSE and REE contents in olivine rims, which is manifested by the reverse zonation for Ti, Zr and Y in olivines (Fig. 6c–e, h–j). Here, we used the olivine/clinopyroxene REE equilibration temperatures to test whether the HFSE and REE in olivine cores were affected by sub-solidus diffusion. The olivine/clinopyroxene REE partition coefficients at varying temperatures (900–1300°C) were calculated following the modelling procedure by Sun and Liang (2012) and Sun and Liang (2013b). The mean major element compositions of olivine and clinopyroxene from Group I, Group II and Group III were selected during the REE partition coefficient calculation. Calculations use a melt water content of 0·2 wt % and pressure of 2 kbar.

Although the olivine/clinopyroxene REE partition coefficients of Hole U1473A olivine gabbros are variable, the mean values of these partition coefficients generally yield olivine/clinopyroxene REE equilibration temperatures varying from 1000 to 1200 °C (Fig. S5). Moreover, the olivine/clinopyroxene REE equilibration temperatures of Group I olivine gabbros are indistinguishable from those of Group II and Group III. Experimental studies suggest the diffusivities of Zr and Ti are slightly slower than REE and Y in olivine (Spandler and O'Neill, 2010). Hence, we suggest that olivine HFSE and REE abundances were not significantly modified by sub-solidus re-equilibration and, thus, most likely recording the magmatic processes.

As shown in Fig. 20a, c, e, AFC processes at high assimilation/crystallization ratios (i.e. r>0·8) can fractionate Zr from REE and Y in minerals more prominently with respect to close-system magmatic processes (i.e. equilibrium crystallization, fractional crystallization, and *in-situ* crystallization). By contrast, without Fe–Ti oxide fractionation, the Ti/REE and Ti/Y fractionations in minerals during AFC processes and close-system processes are indistinguishable (Fig. 20b, d, f).

Clinopyroxene Zr/Nd–Yb (Fig. 20a), olivine Zr/Y–Yb (Fig. 20c), and orthopyroxene Zr/Y–Y correlations (Fig. 20e) are all compatible with AFC processes at high assimilation/crystallization ratios, i.e., r=0·8–0·9 for clinopyroxene and olivine and r=0·7–0·9 for orthopyroxene. Generally, clinopyroxene Ti/Dy–Yb (Fig. 20b), olivine Ti–Y (Fig. 20d), and orthopyroxene Ti–Y correlations (Fig. 20f) are all compatible with oxide-undersaturated magmatic processes (AFC1). Thus, the mineral HFSE/REE fractionations in Group I olivine gabbros are controlled by the extensive reaction with oxide-undersaturated melts at high assimilation rates (r=0·7–0·9).

Mineral HFSE/REE fractionations in olivine gabbros from shear zones (Group II and III): reaction with oxide-saturated melts

Mineral HFSE/REE fractionations in Group II and III olivine gabbros are distinct from those in Group I olivine gabbros, an is summarized as follows:

Downloaded from https://academic.oup.com/petrology/article/61/9/egaa082/5890488 by Institute of Geology and Geophysics, CAS user on 04 March 2021

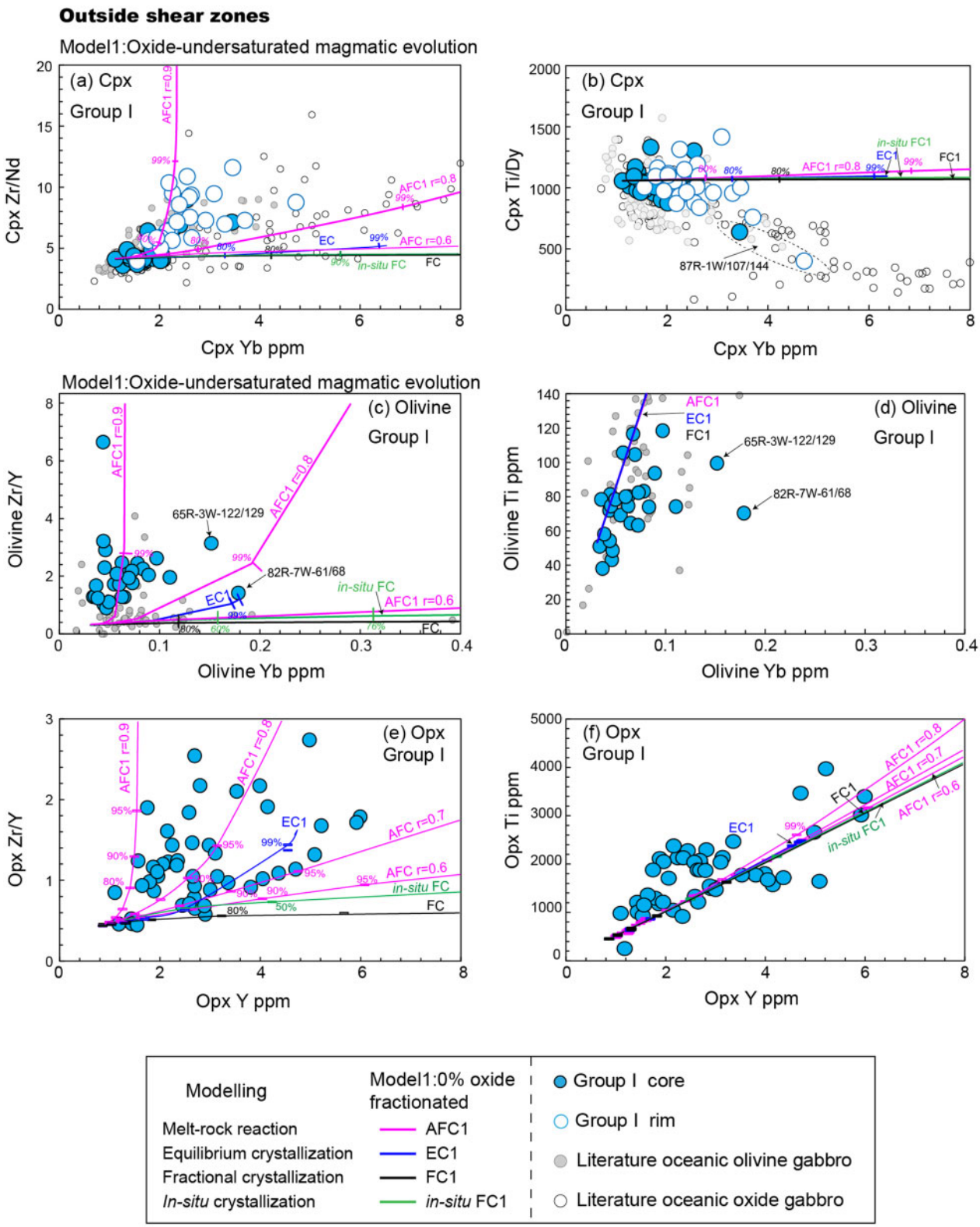

Fig. 20 Geochemical modelling of the HFSE/REE (i.e. Zr/Nd and Ti/Dy ratios) fractionations in (a, b) clinopyroxene (Cpx), (c, d) olivine (Ol) and (e, f) orthopyroxene in Group I olivine gabbros. Model1 corresponds to the melt differentiation (assimilation-fractional crystallization, equilibrium crystallization, fractional crystallization, and *in-situ* crystallization) without ilmenite fractionation. Details of geochemical modelling are given in the text. The parameters, partition coefficients of these modellings are given in Table S9. The italic numbers around each trend represent the degree of fractionation (0–100%). The literature data for the oceanic olivine gabbros and oxide gabbros are from: Hess Deep (East Pacific Rise, EPR) (Lissenberg et al., 2013; Chatterjee, 2017), Atlantis Massif (Mid-Atlantic Ridge, MAR) (Drouin et al., 2009), Godzilla Megamullion (Philippine Sea) (Sanfilippo et al., 2016; Harigane et al., 2019) and Alps ophiolites (Rampone et al., 2016; Sanfilippo et al., 2015b).

Downloaded from https://academic.oup.com/petrology/article/61/9/egaa082/5890488 by Institute of Geology and Geophysics, CAS user on 04 March 2021

1. Group II and III clinopyroxene exhibit decreasing Ti/Dy ratios at decreasing Mg#, similar to oxide gabbro clinopyroxene from other oceanic ridges. By contrast, except for one sample (87R-1W-107/144), Group I clinopyroxene has high and uniform Ti/Dy ratios (Fig. 11c).
2. Plagioclase Ti/Y ratios for Group II and III olivine gabbros remain low and uniform (typically lower than 2200) at the decreasing anorthite contents. This is in contrast to Group I plagioclase, which displays positive correlations of Ti/Y ratios (up to 4776) with anorthite contents (Fig. 11e).
3. Compared to the high and variable Ti/Y and Zr/Y ratios in Group I olivine, Group II and III olivine exhibit low and uniform Ti/Y and Zr/Y ratios (Fig. 9e).
4. Group II and III orthopyroxene exhibit low Ti/Y ratios (typically lower than 700), distinct from the Group I orthopyroxene showing high and variable Ti/Y ratios (up to ~1127, Fig. 12b).

There are abundant textures indicative of dissolution of cumulus minerals (olivine, plagioclase and clinopyroxene) with ilmenite crystallization in Group II and III olivine gabbros (e.g. Fig. 5d, e, h), as discussed above. Fe–Ti oxides (i.e. ilmenite) have very low REE contents (mostly <10 ppb) (She et al., 2015) and thus may efficiently fractionate REE from Ti. Therefore, in this section, in order to assess the processes controlling the mineral HFSE/REE fractionations in Group II and III olivine gabbros, we performed series of geochemical modelling considering various amounts of ilmenite fractionation.

Modelling of oxide-saturated melt-rock reaction

Here, we consider the melt-rock reaction with Fe–Ti oxide (i.e. ilmenite) fractionation:

Oxide-saturated melt-rock reaction (AFC2, AFC3): olivine1 + plagioclase1 + clinopyroxene1 + melt1 = olivine2 + plagioclase2 + clinopyroxenes2 + orthopyroxene + ilmenite + melt2

Partition coefficients for silicate minerals, initial melt compositions, assimilated mineral compositions and the modal mineral proportions for assimilation and crystallization are the same as those applied in the modelling of oxide-undersaturated melt-rock reaction (model 1). Partition coefficients for ilmenite are from Bédard (1994). AFC2 and AFC3 are corresponding to 0·6% and 1·4% Fe–Ti oxide (i.e. ilmenite) fractionation, respectively. Besides, we modelled the equilibrium crystallization (EC), *in-situ* crystallization (*in-situ* FC) and fractional crystallization (FC), considering the 0·6% (model 2) and 1·4% (model 3) Fe–Ti oxide fractionation. Following the *in-situ* crystallization modelling described in Borghini and Rampone (2007), we consider four steps of equilibrium crystallization, where 20%, 40%, 16% and 14·4% of the total trapped melts were consumed in each step. The parameters of geochemical modelling are given in Table S9.

Mineral HFSE/REE fractionations in olivine gabbros from shear zones (Group II and III) controlled by oxide-saturated melt-rock reaction

As shown in Fig. 21, the Fe–Ti oxide fractionation has little effects on the Zr/REE fractionations yet can give rise to prominent Ti/REE fractionations in clinopyroxene, olivine and orthopyroxene. In general, Group II and III clinopyroxene exhibit Zr/Nd–Yb correlations compatible with AFC process at high assimilation/crystallization ratios (r=0·6–0·9). Contrasting with Group I clinopyroxene, Group II and III clinopyroxene show well-defined, negative Ti/Dy–Yb correlations (R^2=0·66), which is compatible with the magmatic processes fractionating Fe–Ti oxide (Fig. 21b). To reconcile the clinopyroxene Zr/Nd–Yb and Ti/Dy–Yb correlations of Group II and III olivine gabbros, ~0·6% Fe–Ti oxide fractionation (model 2) is required (Fig. 21a, b).

Contrasting with Group I olivine, most Group II and III olivine exhibit low and uniform Zr/Y ratios but highly variable Yb contents, which is consistent with AFC processes at lower assimilation/crystallization ratios (r generally lower than 0·8) (Fig. 21c, d). Group II and III olivine define positive Ti–Yb correlations with shallower slopes than Group I and the olivine gabbros from other oceanic ridges, which is consistent with oxide-saturated magmatic processes (Fig. 21e, f). However, the olivine Ti–Yb correlations of Group II and III olivine gabbros cannot be reproduced by AFC process at low assimilation/crystallization ratio (r<0·8), assuming ~0·6% Fe–Ti oxide fractionation (model 2) (Fig. 21c, e). Instead, ~1·4% Fe–Ti oxide fractionation (model 3) is required to reconcile the Ti–Yb and Zr/Y–Yb correlations of Group II and III olivine (Fig. 21d, f).

Group II and III orthopyroxene show a shallow slope for the Zr/Y–Y correlations (Fig. 21g), which can be reproduced by AFC processes at low assimilation/crystallization ratio (r<0·8). Particularly, orthopyroxene from a few samples exhibits low Zr/Y ratios (i.e. ~0·5) but high Y contents (3–5ppm), following the fractional crystallization trend (Fig. 21g). In addition, Group II and III orthopyroxene exhibit shallow slopes for Ti–Y correlations, which is consistent with oxide-saturated evolution (Fig. 21h). To reproduce both the orthopyroxene Ti–Y and Zr/Y–Y correlations of Group II and III olivine gabbros, we find ~0·6% Fe–Ti oxide fractionation was required (Fig. 21g, h).

The amount of Fe–Ti oxide fractionation inferred from orthopyroxene is compatible with results from clinopyroxene (~0·6% oxide fractionation, Fig. 21a, b) yet are higher than those from olivine (~1·4% oxide fractionated, Fig. 21e, f). Such trace element differences between orthopyroxene and olivine are not compatible with their close textural associations (e.g. Fig. 5c, i). A possible explanation is that the olivine grains have reset their compositions by the diffusive exchange with more evolved residual melts that can fractionate more Fe–Ti oxides after orthopyroxene crystallization, due to the

Downloaded from https://academic.oup.com/petrology/article/61/9/egaa082/5890488 by Institute of Geology and Geophysics, CAS user on 04 March 2021

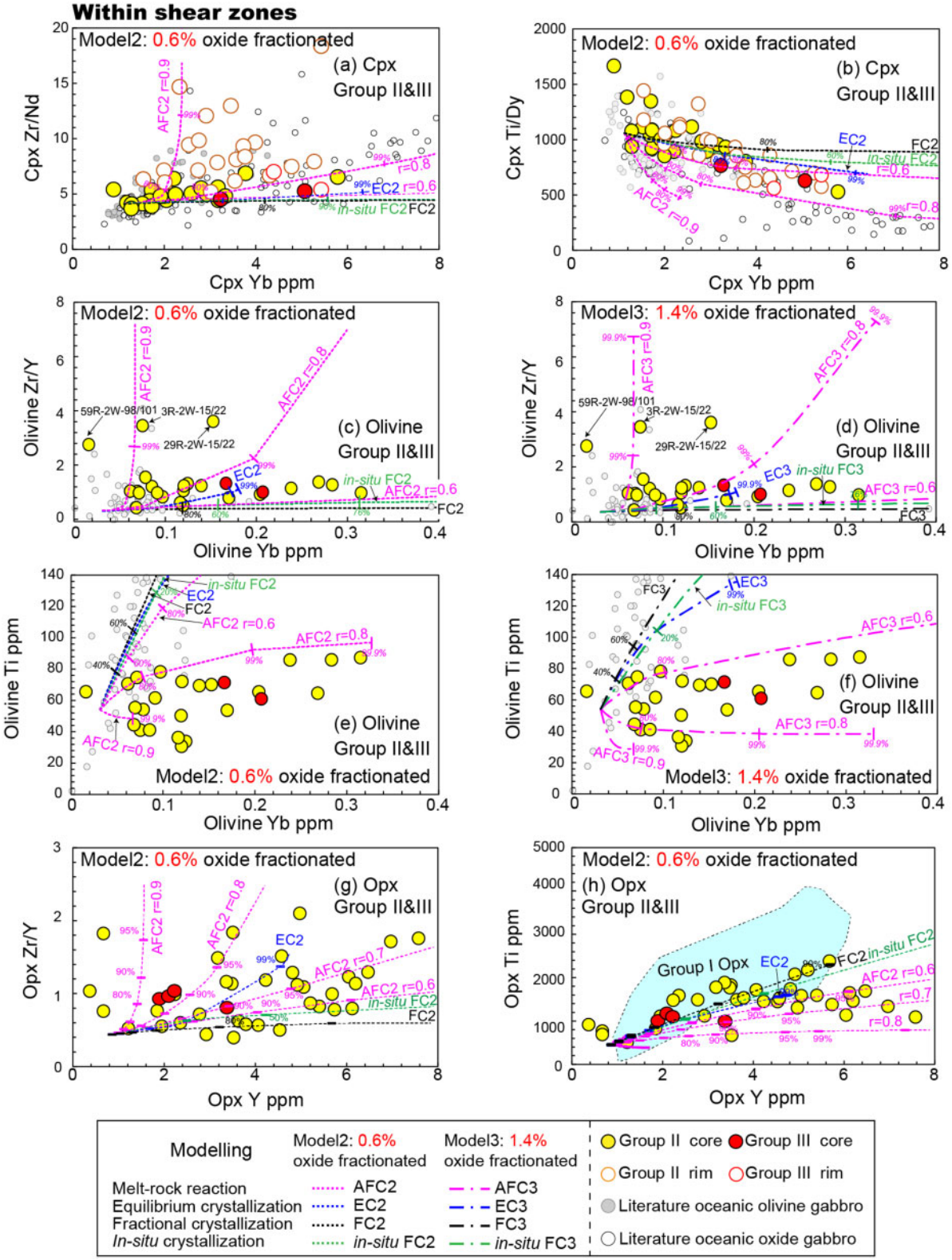

Fig. 21 Geochemical modelling reproducing the HFSE/REE (Ti/Y and Zr/Y) fractionations in clinopyroxene (Cpx, a, b), olivine (Ol) (c–f) and orthopyroxene (g, h). Model2 and model3 are corresponding to the melt differentiation (assimilation-fractional crystallization, equilibrium crystallization, fractional crystallization, and *in-situ* crystallization) producing 0·6% and 1·4% Fe–Ti oxide (i.e. ilmenite), respectively. Details of geochemical modelling are given in the text. The parameters and partition coefficients of these modellings are given in Table S9. The italic numbers around each trend represent the degree of fractionation (0–100%). Literature data for the oceanic olivine gabbros and oxide gabbros are from: Hess Deep (East Pacific Rise, EPR) (Lissenberg et al., 2013; Chatterjee, 2017), Atlantis Massif (Mid-Atlantic Ridge, MAR) (Drouin et al., 2009), Godzilla Megamullion (Philippine Sea) (Sanfilippo et al., 2016; Harigane et al., 2019) and Alps ophiolites (Rampone et al., 2016; Sanfilippo et al., 2015b).

Downloaded from https://academic.oup.com/petrology/article/61/9/egaa082/5890488 by Institute of Geology and Geophysics, CAS user on 04 March 2021

fast diffusion rates for HFSE and REE in olivine (Spandler and O'Neill, 2010; Spandler et al., 2007).

For Group II and III olivine gabbros, HFSE (i.e. Ti and Zr) and REE in orthopyroxene and olivine are compatible with the AFC process at lower assimilation rates (i.e. r<0·8, Fig. 21c–h) with respect to those in clinopyroxene (i.e. r=0·6–0·9, Fig. 21a, b). This feature cannot be explained by the uncertainties resulting from the adopted parameters in the modelling or the contrasting reactivities of various minerals, as the assimilation/crystallization ratios inferred from Group I orthopyroxene and olivine (r=0·7–0·9) are compatible with those deduced from Group I clinopyroxene (r=0·8–0·9) (Fig. 20). One possible explanation is the prolonged diffusive exchange between olivine and residual melts and the prolonged crystallization of orthopyroxene in Group II and III olivine gabbros due to the high fraction of residual melts in Group II and III olivine gabbros, i.e., TMF of ~6% for Group II and III and ~3% for Group I (Fig. 19a). In this scenario, the HFSE/REE fractionations in many Group II and III orthopyroxene and olivine might reflect the melts at lower temperatures than those crystallizing clinopyroxene. The lower assimilation rates deduced from the HFSE/REE fractionations in orthopyroxene and olivine probably reflect the decreasing porosity of crystal mush in the final crystallization stage.

Taken as a whole, we find the mineral HFSE/REE fractionations in Group II and III olivine gabbros are compatible with the oxide-saturated melt-rock reaction at variable assimilation rates.

Ti and REE in plagioclase: Records of reaction with two distinct melts

A temperature-dependent AFC model to reproduce the REE fractionations in clinopyroxene and plagioclase

The LREE/HREE fractionations in plagioclase are clearly distinct with respect to those in clinopyroxene in Hole U1473A olivine gabbros. For instance, plagioclase generally exhibits normal Ce zonation but slightly reverse Y zonation (Fig. 10h, i), whereas clinopyroxene typically shows normal zonation for both Ce and Y (Fig. 10d, e). Moreover, plagioclase exhibit poorly-defined Ce–Y correlations (R^2=0·06), whereas clinopyroxene display well-defined, positive Ce–Y correlations (R^2=0·86) (Fig. 11d, f). Such contrasts likely reflect the cooling effects on the REE partitioning between clinopyroxene and plagioclase. For instance, following the model of Sun et al. (2017), the plagioclase-melt partition coefficients of Ce and Y can decrease from 0·1 to 0·03 and from 0.02 to 0·005 with the temperatures decreasing from 1150 to 1050°C, respectively. By contrast, following the Sun and Liang (2012)'s model, the clinopyroxene-melt partition coefficients of Ce and Y slightly increase from 0·13 to 0·17 and from 0·62 to 0·98 with temperatures decreasing from 1150 to 1050°C, respectively. Therefore, we performed a temperature-dependent geochemical modelling (model 4) to reproduce the REE fractionation in both clinopyroxene and plagioclase.

As ilmenite contains extremely low REE contents (e.g. She et al. (2015)), we ignore the effects of ilmenite fractionation on REE fractionations. The REE partition coefficients for clinopyroxene, olivine, plagioclase and orthopyroxene are calculated based on the published models (Sun et al., 2017; Sun and Liang, 2013a, b; Yao et al., 2012), using the corresponding mineral compositions for sample 65R-3W-122/129 to better fit the general trends, pressure of 2 kbar, and water content of 0·2 wt.%. We calculate series of mineral-melt partition coefficients at temperatures varying from 1150 to 1010°C. The residual melt mass at various temperatures are constrained by the fractional crystallization modelling of primary MORB (compositions are from the most MgO-rich Atlantis Bank basalts (Coogan et al., 2004)) using PELE programmed by Alan E. Boudreau (http://www.nicholas.duke.edu/people/faculty/boudreau/DownLoads.html). During the modelling, we assume seven steps of crystallization. Following the same methods and boundary conditions described in the previous section, we calculate the trends of equilibrium crystallization, fractional crystallization, and AFC processes. The parameters of modelling (model 4) are given in Table S10.

As shown in Fig. 22, the Ce/Y–Y correlations for both clinopyroxene and plagioclase can be successfully reproduced by the AFC processes at assimilation/crystallization ratios (r) of 0·7–0·9 for Group I and 0·6–0·9 for Group II and III olivine gabbros (Fig. 22), which is consistent with the modellings of clinopyroxene HFSE/REE fractionations (Fig. 20a, b and Fig. 21a, b). As plagioclase and clinopyroxene are the major rock-forming minerals in the lower oceanic crust, we suggest the dominant magmatic processes, during the emplacement of the Atlantis Bank gabbroic massif, were AFC processes induced by porous melt flow through the lower oceanic crust.

Ti/REE fractionation in plagioclase: records of two distinct melt-rock reaction

In Hole U1473A olivine gabbros, plagioclase exhibits Ti/Y–Ce correlations distinct from clinopyroxene. For instance, plagioclase in Group II and III olivine gabbros exhibit low and uniform Ti/Y ratios with the increasing in Ce contents, whereas clinopyroxene displays negative Ti/Y–Ce correlations (Fig. 23). Again, these contrasts are likely related to the changes in Ti and REE partitioning between clinopyroxene and plagioclase during cooling. Unfortunately, the lattice strain models for the HFSE (i.e. Ti and Zr) partitioning between plagioclase and clinopyroxene are poorly constrained (Sun et al., 2017), which makes the quantitative modelling of the HFSE/REE fractionations in plagioclase unreliable. However, Group II and III plagioclase exhibit the Ti/Y–Ce correlations contrasting with Group I, implying the reaction with different melts.

Downloaded from https://academic.oup.com/petrology/article/61/9/egaa082/5890488 by Institute of Geology and Geophysics, CAS user on 04 March 2021

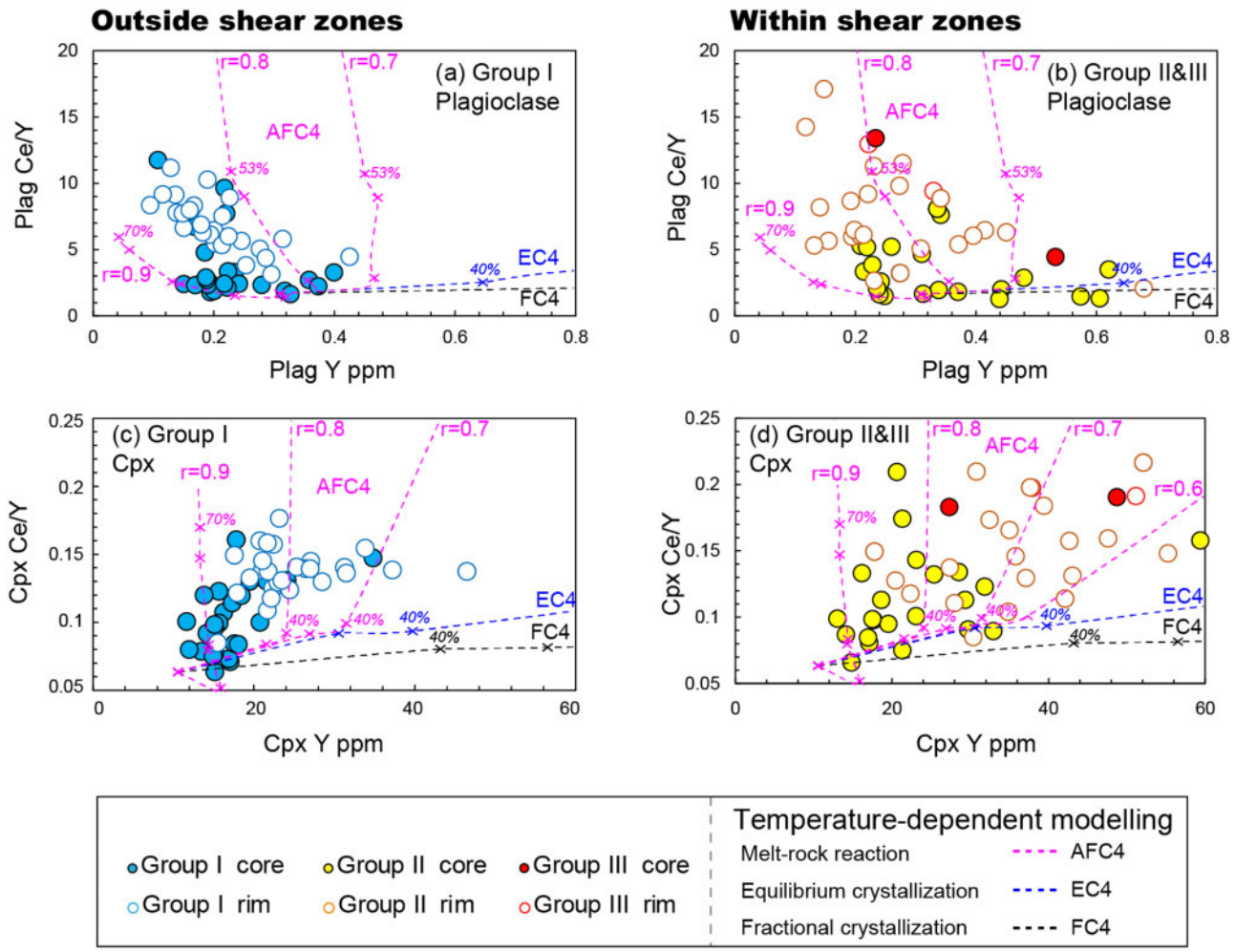

Fig. 22 Temperature-dependent geochemical modelling reconciling the Ce/Y fractionation in (a,b) plagioclase (Plag) and (c, d) clinopyroxene (Cpx). In these models, we consider the effects of cooling on the REE partitioning among minerals. Details of the models are given in the text and the parameters are given in Table S10. The italic numbers around each trend represent the degree of crystallization (0–100%).

Group I plagioclase exhibits increasing Ti/Y ratios and Ce contents from cores to rims, which is distinct from the plagioclase in oxide gabbros from other oceanic ridges (Fig. 23a). In comparison, Group II and III plagioclase have low and uniform Ti/Y ratios for both cores and rims, quite similar to plagioclase in oceanic oxide gabbros (Fig. 23b). This implies the involvements of oxide-saturated melts during the crystallization of Group II and III plagioclase rims. Overall, we suggest Group I plagioclase was formed through the extensive reaction with oxide-undersaturated melts, while Group II and III plagioclase experienced the modification by oxide-saturated melts.

Contrasting reaction history of olivine gabbros from less deformed zones and shear zones

Olivine gabbros from the less deformed zones (i.e. Group I olivine gabbros from 589–809 mbsf) of Hole U1473A are characterized by (1) low modal orthopyroxene, Fe–Ti oxide and brown amphibole (Fig. S1b); (2) abundant dissolution-precipitation textures (e.g. olivine, plagioclase, and clinopyroxene) (Fig. 4a–c) but near absence of textures related to ilmenite precipitation; and (3) mineral HFSE/REE fractionations compatible with the Fe–Ti oxide-undersaturated melt-rock reaction processes (Fig. 20). These characteristics indicate these gabbros experienced the reaction with oxide-undersaturated melts. We find no evidence for the significant involvement of oxide-saturated melts during the formation of the Group I olivine gabbros.

However, a range of petrological and mineral trace-element features of the olivine gabbros from the pervasively deformed intervals (Group II and III) are consistent with the extensive hybridization by late-stage, oxide-saturated melts: (1) the high modal ilmenite and brown amphibole (Fig. S1b); (2) the textures indicative of dissolution of cumulus minerals with crystallization of ilmenite (Fig. 5d, h, e); (3) mineral Ti/REE fractionation deviated from the oxide-undersaturated melt differentiation trends (Fig. 21); and (4) the whole-rock

Downloaded from https://academic.oup.com/petrology/article/61/9/egaa082/5890488 by Institute of Geology and Geophysics, CAS user on 04 March 2021

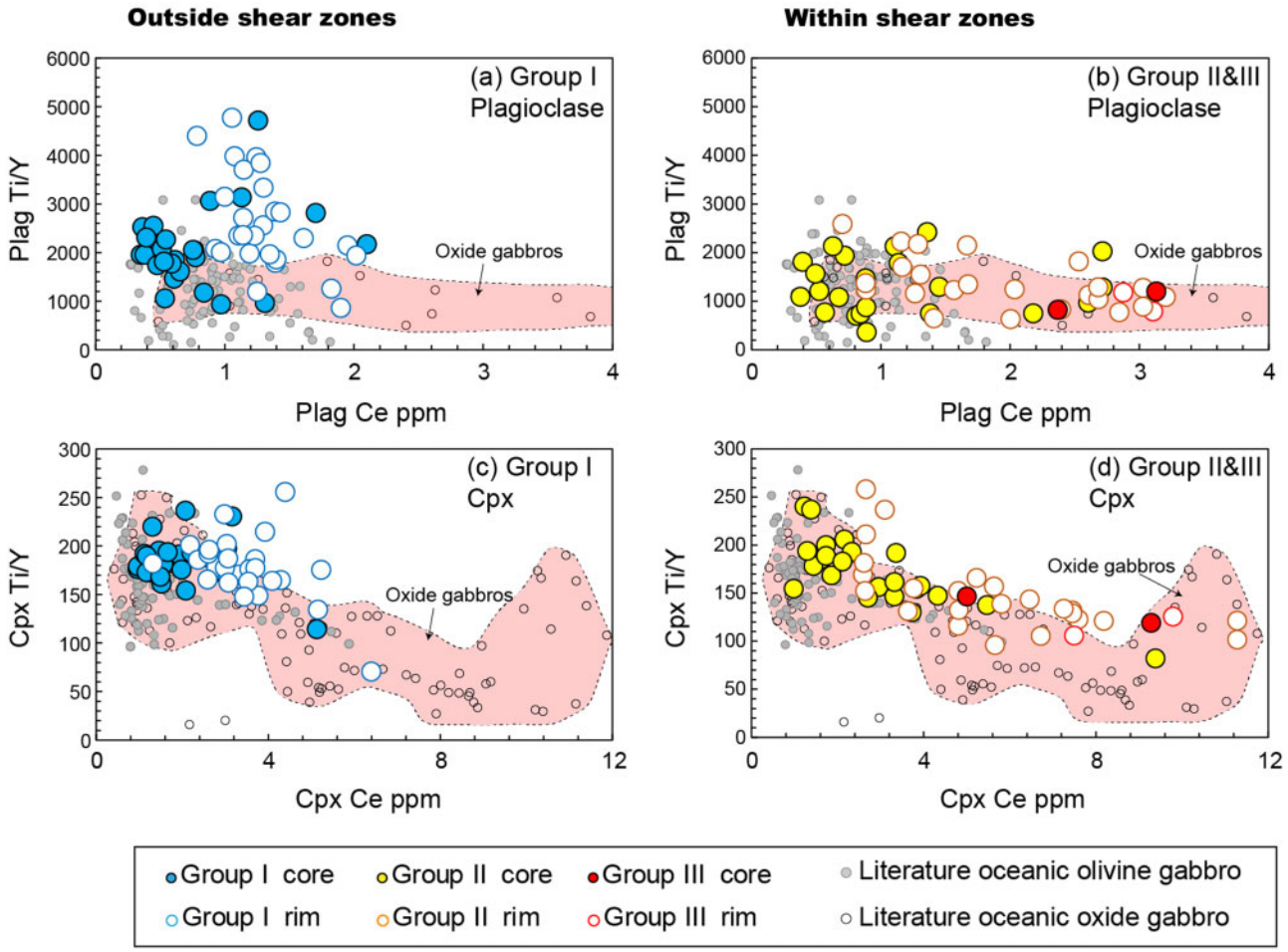

Fig. 23 (a, b) Plagioclase (Plag) Ti/Y ratios plotted against Ce contents and (c, d) clinopyroxene (Cpx) Ti/Y ratios plotted against Ce contents. The literature data for the oceanic olivine gabbros and oxide gabbros are from: Hess Deep (East Pacific Rise, EPR) (Lissenberg et al., 2013), Atlantis Massif (Mid-Atlantic Ridge, MAR) (Drouin et al., 2009), Godzilla Megamullion (Philippine Sea) (Sanfilippo et al., 2016; Harigane et al., 2019).

Ti/REE fractionations compatible with the entrapment of oxide-saturated melts (Fig. 19c). The HFSE/REE fractionations in different minerals are consistent with the reaction of gabbros with oxide-saturated melts at various assimilation rates (Fig. 21 and Fig. 23).

However, textures of Group II and III olivine gabbros indicate the olivine gabbros from shear zones underwent multi-stage melt-rock reaction. For instance, there are abundant textures indicative of the reaction with oxide-undersaturated melts in Group II and III olivine gabbros, i.e., the growth of poikilitic clinopyroxene against plagioclase (Fig. 5a) and large clinopyroxene enclosing corroded remnants of small olivine grains (Fig. 5b). In addition, in Group II olivine gabbros, there are large clinopyroxene oikocrysts, either with irregular contacts against olivine and plagioclase or enclosing resorbed plagioclase (Fig. 18a, b, e, f), indicating the reaction with oxide-undersaturated melts. The rims of these clinopyroxene oikocrysts were partially corroded and exhibit irregular contacts against interstitial ilmenites and brown amphiboles (Fig. 18c, d, g, h), indicating the textures related to early reactions were overprinted by the oxide-saturated melt percolation. Therefore, we suggest at least Group I and II olivine gabbros both underwent an early-stage reaction with oxide-undersaturated melts. For Groups II olivine gabbros, this previous event was overprinted during the late-stage hybridization by oxide-saturated melts.

Temporal and spatial evolution of multi-stage melt transport through the Atlantis Bank gabbroic massif

Several lines of evidence outlined above suggest that Atlantis Bank olivine gabbros have experienced a complex history including (1) early-stage reaction with a moderately fractionated melt (oxide-undersaturated) and (2) late-stage reaction with a highly evolved, oxide-saturated melt. Only olivine gabbros from shear zones (i.e. Group II and III olivine gabbros) record both stages of reaction, whereas those outside shear zones (Group I olivine gabbros) merely exhibit geochemical signatures of early-stage melt-rock reaction. We postulate that de-

Downloaded from https://academic.oup.com/petrology/article/61/9/egaa082/5890488 by Institute of Geology and Geophysics, CAS user on 04 March 2021

formation might not play a role in early-stage melt migration, as the textures indicative of early-stage melt-rock reactions are common in the olivine gabbros from both less deformed (Group I) and pervasively deformed intervals (Group II) (Fig. 4a-c, Fig. 5a, b, g and Fig. 18a, b, e, f). Instead, early-stage melt migration was most likely a consequence of crystal mush compaction (Lissenberg & Macleod, 2016; Lissenberg et al., 2013), as evidenced by the abundant compaction textures in less deformed gabbros (e.g. Fig. 4e, f). In contrast, late-stage melt transport is inextricably coupled to syn-magmatic deformation, which will provide melt conduits (i.e. shear zones) and pressure gradients that may promote melt flow.

Early-stage compaction-driven melt transport

Compaction-driven porous melt migration is the natural consequence of a crystal mush-dominated magma plumbing system (e.g., Lissenberg & Macleod, 2016, Lissenberg et al., 2019). In this scenario, melt migration by buoyancy-driven porous flow would lead to reactions between melt and surrounding crystal framework (Lissenberg et al., 2019). Textural observations imply that most olivine gabbros, regardless of their associations with shear zones, record the early-stage reaction with an oxide-undersaturated melt. Thus, the compaction-driven porous melt flow might be pervasive in Atlantis Bank lower crust. The textures and geochemical modelling coherently show that most minerals in olivine gabbros from less deformed zones (Group I) interacted with oxide-undersaturated melts, implying that, for olivine gabbros, compaction led to efficient melt extraction before the system reached oxide saturation.

Late-stage deformation-driven melt transport

The Atlantis Bank gabbroic massif exhibits strong lateral variability of crustal architecture from a central olivine gabbro/troctolite core to peripheral highly evolved oxide gabbro, indicating extensive lateral and vertical transport of oxide-saturated melts (Dick et al., 2019a; Dick et al., 2019b). The oxide-rich nature of the gabbroic massif's margins makes understanding the mechanism of oxide-saturated melt transport critical to unravel the origin of its compositional zonation.

Our data show that only the olivine gabbros within shear zones (Group II and III) underwent oxide-saturated melt-rock reaction, whereas those outside shear zones (Group I) were merely hybridized by oxide-undersaturated melts. This observation can be explained by either the ductile deformation localized in the gabbros with high fractions of oxide-saturated melts or the porous melt transport through the ductile shear zones (Kelemen et al., 1995; Hasalová et al., 2008; Meek et al., 2019). As even the most Fe–Ti-rich melts are more buoyant than the gabbros (e.g., Natland et al., 2001), buoyancy-driven compaction concentrates late melts near the intrusive margins at porosity and/or thermal boundaries (i.e. the 90 and 300 mbsf major element discontinuities in Hole U1473A, Fig. 14). Oxide-saturated melts was limited to the pervasively deformed interval of 0–589 mbsf (Group II) and a few small shear zones below 589 mbsf (Group III). However, no major element discontinuity is present near 589 mbsf, indicating it was not an intrusive margin that may have acted as a melt trap. Hence, ductile deformation of partially molten gabbro may have triggered the percolation of oxide-saturated melts in Group II and III olivine. Considering the significant thickness of the oxide-saturated melt infiltration zone (0–589 mbsf), we suggest that syn-magmatic deformation, creating additional permeability in the partially molten rocks (e.g., Holtzman and Kohlstedt, 2007; Kaczmarek and Müntener, 2008; Meeks et al., 2019), triggered the large-scale permeable transport of oxide-saturated melts through the lower oceanic crust. This process is critical to generate the compositional zonation of the Atlantis Bank gabbroic massif.

Melt transport history of the Atlantis Bank gabbroic massif

Taken as a whole, there were two stages of melt migration for each intrusion within the Atlantis Bank gabbroic massif, the initial compaction-driven melt migration in deep lower crust followed by the deformation-driven melt migration in high-level crystal-plastic regime (Dick et al., 2019a, b). During the initial emplacement, compaction-driven melt migration occurred (Fig. 24a), producing the upward differentiation trend in each intrusion. This stage involves high volume of primitive to modestly evolved melt transport. Meanwhile, the melt-rock reaction due to the chemical disequilibrium during melt transport preferentially enriched the migrating melts in more incompatible trace elements (Lissenberg et al., 2013). As transported to the high-level crystal–plastic regime, syn-magmatic deformation gave rise to the abundant shear zones crosscutting primary intrusions (Fig. 24b). The volumetrically minor oxide-saturated melts were then localized into shear zones and were then permeably transported by the ongoing deformation. Sheared gabbros provided paths for the kilometre-scale transport of oxide-saturated melt, leading the way for extensive melt hybridization. With the increase in evolved melt fractions to the margins of Atlantis Bank gabbroic massif, the less evolved gabbros were transformed to oxide gabbros, giving rise to its compositional zonation (Dick et al., 2019a,b).

CONCLUSIONS

Mineral trace element compositions of IODP Hole U1473A olivine gabbros are strongly correlated with their spatial associations with ductile shear zones. Olivine gabbros outside shear zones (Group I) exhibit geochemical features of oxide-undersaturated melt-rock reaction, whereas those within shear zones (Group II and III) display additional signatures of oxide-

Downloaded from https://academic.oup.com/petrology/article/61/9/egaa082/5890488 by Institute of Geology and Geophysics, CAS user on 04 March 2021

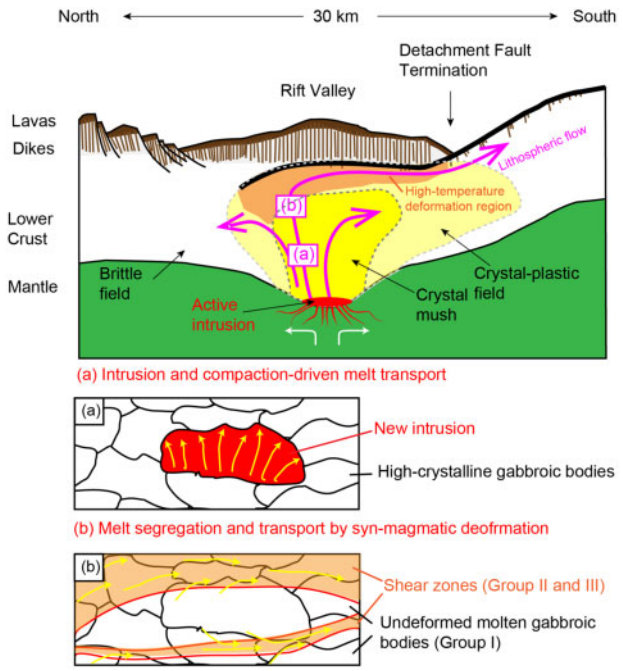

Fig. 24 Cartoons illustrating the tectonic and magmatic evolution of Atlantis Bank lower oceanic crust. Each small intrusion would diapirically rise with lithospheric flow. Initially, there was compaction-driven melt transport that was limited by the permeability barrier near the intrusive boundary, forming the upward differentiation trend in each intrusion. (a) Oxide-undersaturated melt-rock reaction occurred in this stage, preferentially enriching the melt in more incompatible trace elements. (b)As migrated to the crystal-plastic regime, syn-magmatic deformation gave rise to numerous shear zones crosscutting the gabbroic bodies and opened the permeability of sheared gabbros, giving rise to the large-scale both vertical and lateral melt transport. Pink arrows represent the lithospheric flow. Yellow arrows in (a) and (b) represent porous melt flow in different stages.

saturated melt-rock reaction. These observations reflect two stages of permeable melt transport through the 660-km^2 Atlantis Bank gabbroic massif following intrusion of local gabbro plutons. Early-stage, oxide-undersaturated melt transport was compaction-driven, while late-stage, oxide-saturated melt migration was triggered by syn-magmatic deformation. Gabbroic shear zones provide conduits for large-scale evolved melt transport, giving rise to significant compositional and geochemical zonation. Such multi-stage melt migration due to compaction and syn-magmatic deformation are essential features of crustal accretion at the Atlantis Bank, reflecting unusually high magma supply compared to crustal accretion at lower magma-supply localities, e.g., Atlantis Massif (MAR) (Blackman et al., 2006; Godard et al., 2009).

ACKNOWLEDGEMENT

We would like to thank Professor Valentin Troll and Professor Georg Zellmer for their editorial handling. The paper benefits from reviews by Dr. Basch Valentin and other three anonymous reviewers. We thank Hong-Yue Wang, Ding-Shuai Xue and Yan-Hong Liu for their help in whole-rock major element analysis, Di Zhang for assistance with EPMA, and Shi-Tou Wu for LA-ICP-MS analysis. Benjamin Urann is thankful for his help in the manuscript preparation. Chuan-Zhou Liu thanks the IODP-CHINA office for providing the opportunity to participate the Expedition 360.

FUNDING

Foundation of Strategic Priority Research Program of the Chinese Academy of Sciences (XDB42020301), National Natural Science Foundation of China (41673038) and the Laboratory for Marine Geology, Qingdao National Laboratory for Marine Science and Technology (MGQNLM201702). Financial support for H.J.B. Dick was provided by the US National Science Foundation Grant # OCE-1637130.

SUPPLEMENTARY DATA

Supplementary data including Fig. S1 to S5 and Table S1 to S10 are available at Journal of Petrology online.

REFERENCES

Baines, A. G., Cheadle, M. J., Dick, H. J. B., Scheirer, A. H., John, B. E., Kusznir, N. J. & Matsumoto, T. (2007). Evolution of the Southwest Indian Ridge from 55°45′E to 62°E: Changes in plate-boundary geometry since 26 Ma. *Geochemistry, Geophysics, Geosystems* **8**.

Baines, A. G., Cheadle, M. J., John, B. E. & Schwartz, J. J. (2008). The rate of oceanic detachment faulting at Atlantis Bank, *SW Indian Ridge. Earth & Planetary Science Letters* **273**, 105–114.

Basch, V., Rampone, E., Crispini, L., Ferrando, C., Ildefonse, B. & Godard, M. (2018). From mantle peridotites to hybrid troctolites: Textural and chemical evolution during melt-rock interaction history (Mt. Maggiore, Corsica, France). *Lithos* **323**, 4–23.

Bédard, J. H. (1994). A procedure for calculating the equilibrium distribution of trace elements among the minerals of cumulate rocks, and the concentration of trace elements in the coexisting liquids. *Chemical Geology* **118**, 143–153.

Bédard, J. H. (2010). Parameterization of the Fe–Mg exchange coefficient (Kd) between clinopyroxene and silicate melts. *Chemical Geology* **274**, 169–176.

Blackman, D. K., Ildefonse, B., John, B. E., Ohara, Y., Miller, D. J., Macleod, C. J. & Morris, A. (2006). Oceanic Core Complex Formation, *Atlantis Massif. Scientific Drilling* **1**, 28.

Bloomer, S., Meyer, P., Dick, H., Ozawa, K. & Natland, J. (1991). Textural and mineralogic variations in gabbroic rocks from Hole 735B. *Von Herzen, RP, Robinson, PT, et al., Proc. ODP, Sci. Results*, 21–39.

Borghini, G., Rampone, E. (2007). Postcumulus processes in oceanic-type olivine-rich cumulates: the role of trapped melt crystallization versus melt/rock interaction. *Contributions to Mineralogy & Petrology*, **154**, 619–633.

Botcharnikov, R. E., Almeev, R. R., Koepke, J. & Holtz, F. (2008). Phase Relations and Liquid Lines of Descent in Hydrous Ferrobasalt—Implications for the Skaergaard Intrusion and Columbia River Flood Basalts. *Journal of Petrology* **49**, 1687–1727.

Downloaded from https://academic.oup.com/petrology/article/61/9/egaa082/5890488 by Institute of Geology and Geophysics, CAS user on 04 March 2021

Brunelli, D., Sanfilippo, A., Bonatti, E., Skolotnev, S., Escartin, J., Ligi, M., Ballabio, G. & Cipriani, A. (2020). Origin of oceanic ferrodiorites by injection of nelsonitic melts in gabbros at the Vema Lithospheric Section, *Mid Atlantic Ridge. Lithos* 368–369, 105589.

Cannat, M., Ceuleneer, G. & Fletcher, J. (1997). Localization of ductile strain and the magmatic evolution of gabbroic rocks drilled at the Mid-Atlantic Ridge (23°N). In *Proceedings-Ocean Drilling Program Scientific Results* (pp. 77–98). National Science Foundation.

Cannat, M., Sauter, D., Mendel, V. r., Ruellan, E., Okino, K., Escartin, J., Combier, V. & Baala, M. (2006). Modes of seafloor generation at a melt-poor ultraslow-spreading ridge. *Geology* **34**, 605–608.

Carbotte, S. M., Marjanović, M., Carton, H., Mutter, J. C., Canales, J. P., Nedimović, M. R., Han, S. & Perfit, M. R. (2013). Fine-scale segmentation of the crustal magma reservoir beneath the East Pacific Rise. *Nature Geoscience* **6**, 866–870.

Chatterjee, S. (2017). *Petrological and geochemical characteristics of gabbros drilled at IODP site 1415: Evidence for an enriched mantle*. Hokkaido University.

Chen, Y., Niu, Y., Wang, X., Gong, H., Guo, P., Gao, Y. & Shen, F. (2019). Petrogenesis of ODP Hole 735B (Leg 176) Oceanic Plagiogranite: Partial Melting of Gabbros or Advanced Extent of Fractional Crystallization? *Geochemistry, Geophysics, Geosystems* **20**, 2717–2732.

Ciazela, J. (2018). *Sulfide differentiation in slow-spreading ridge magmas*. Hannover: Institutionelles Repositorium der Leibniz Universität.

Collier, M. L. & Kelemen, P. B. (2010). The Case for Reactive Crystallization at Mid-Ocean Ridges. *Journal of Petrology* **51**, 1913–1940.

Coogan, L. A. (2014). *4.14 - The Lower Oceanic Crust. In:* Turekian, K. K. (ed.) Treatise on Geochemistry (Second Edition). Oxford: Elsevier, 497–541.

Coogan, L. A., Jenkin, G. R. T. & Wilson, R. N. (2007). Contrasting Cooling Rates in the Lower Oceanic Crust at Fast- and Slow-spreading Ridges Revealed by Geospeedometry. *Journal of Petrology* **48**, 2211–2231.

Coogan, L. A., MacLeod, C. J., Dick, H. J. B., Edwards, S. J., Kvassnes, A., Natland, J. H., Robinson, P. T., Thompson, G. & O'Hara, M. J. (2001a). Whole-rock geochemistry of gabbros from the Southwest Indian Ridge: constraints on geochemical fractionations between the upper and lower oceanic crust and magma chamber processes at (very) slow-spreading ridges. *Chemical Geology* **178**, 1–22.

Coogan, L. A., Saunders, A. D., Kempton, P. D. & Norry, M. J. (2000). Evidence from oceanic gabbros for porous melt migration within a crystal mush beneath the Mid-Atlantic Ridge. *Geochemistry, Geophysics, Geosystems* **1**.

Coogan, L. A., Thompson, G. M., MacLeod, C. J., Dick, H. J. B., Edwards, S. J., Hosford Scheirer, A. & Barry, T. L. (2004). A combined basalt and peridotite perspective on 14 million years of melt generation at the Atlantis Bank segment of the Southwest Indian Ridge: evidence for temporal changes in mantle dynamics? *Chemical Geology* **207**, 13–30.

Coogan, L. A., Wilson, R. N., Gillis, K. M. & Macleod, C. J. (2001b). Near-solidus evolution of oceanic gabbros: insights from amphibole geochemistry. *Geochimica et Cosmochimica Acta* **65**, 4339–4357.

Cortesogno, L., Gaggero, L. & Zanetti, A. (2000). Rare earth and trace elements in igneous and high-temperature metamorphic minerals of oceanic gabbros (MARK area, Mid-Atlantic Ridge). *Contributions to Mineralogy and Petrology* **139**, 373–393.

DePaolo, D. J. (1981). Trace element and isotopic effects of combined wallrock assimilation and fractional crystallization. *Earth and Planetary Science Letters* **53**, 189–202.

Detrick, R. S., Mutter, J. C., Buhl, P. & Kim, I. I. (1990). No evidence from multichannel reflection data for a crustal magma chamber in the MARK area on the Mid-Atlantic Ridge. *Nature* **347**, 61–64.

Dick, H. J. B. (1991). Tectonic evolution of the Atlantis II fracture zone. *Proceedings of the Ocean Drilling Program Scientific Results* **118**.

Dick, H. J. B., Kazuhito, O., S., M. P., Yaoling, N., T., R. P., Marc, C., Rejean, H., Jinichiro, M., H., N. J., Gregory, H. J. & M., M. S. (2002). Primary silicate mineral chemistry of a 1.5-km section of very slow spreading lower ocean crust: ODP Hole 735B, Southwest Indian Ridge. *Proceedings of the Ocean Drilling Program Scientific Results* **176**, 1–61.

Dick, H. J. B., Kvassnes, A. J. S., Robinson, P. T., Macleod, C. J. & Kinoshita, H. (2019a). The Atlantis Bank Gabbro Massif, Southwest Indian Ridge. *Progress in Earth and Planetary Science* **6**, **1**–70.

Dick, H. J. B., Lin, J. & Schouten, H. (2003). An ultraslow-spreading class of ocean ridge. *Nature* **426**, 405–412.

Dick, H. J. B., MacLeod, C. J., Blum, P., and the Expedition 360 Scientists. (2015). Southwest Indian Ridge Lower Crust and Moho: The nature of the lower crust and Moho at slower spreading ridges (SloMo-Leg 1). International Ocean Discovery Program Scientific Prospectus, 360. doi: 10.14379/iodp.sp.360.2015

Dick, H. J. B., MacLeod, C. J., Blum, P., Abe, N., Blackman, D. K., Bowles, J. A., Cheadle, M. J., Cho, K., Ciazela, J., Deans, J. R., Edgcomb, V. P., Ferrando, C., France, L., Ghosh, B., Ildefonse, B. M., Kendrick, M. A., Koepke, J. H., Leong, J. A. M., Liu, C., Ma, Q., Morishita, T., Morris, A., Natland, J. H., Nozaka, T., Pluemper, O., Sanfilippo, A., Sylvan, J. B., Tivey, M. A., Tribuzio, R. & Viegas, L. G. F. (2017). Expedition 360 summary. *In MacLeod, C.J., Dick, H.J.B., Blum, P., and the Expedition 360 Scientists, Southwest Indian Ridge Lower Crust and Moho. Proceedings of the International Ocean Discovery Program, 360. College Station, TX (International Ocean Discovery Program)*.

Dick, H. J. B., MacLeod, C. J., Blum, P., Abe, N., Blackman, D. K., Bowles, J. A., Cheadle, M. J., Cho, K., Ciążela, J., Deans, J. R., Edgcomb, V. P., Ferrando, C., France, L., Ghosh, B., Ildefonse, B., John, B., Kendrick, M. A., Koepke, J., Leong, J. A. M., Liu, C., Ma, Q., Morishita, T., Morris, A., Natland, J. H., Nozaka, T., Pluemper, O., Sanfilippo, A., Sylvan, J. B., Tivey, M. A., Tribuzio, R. & Viegas, G. (2019b). Dynamic accretion beneath a slow-spreading ridge segment: IODP Hole 1473A and the Atlantis Bank Oceanic Core Complex. *Journal of Geophysical Research: Solid Earth* **124**, 12631–12659.

Dick, H. J. B., Meyer, P. S., Bloomer, S. H., Kirby, S. H., Stakes, D. S. & Mawer, C. (1991). Lithostratigraphic evolution of an in-situ section of oceanic layer 3. *Proceedings of the Ocean Drilling Program Scientific Results* **118**.

Dick, H. J. B., Natland, J. H., Alt, J. C., Bach, W., Bideau, D., Gee, J. S., Haggas, S., Hertogen, J. G. H., Hirth, G. & Holm, P. M. (2000). A long in situ section of the lower ocean crust: results of ODP Leg 176 drilling at the Southwest Indian Ridge. *Earth & Planetary Science Letters* **179**, 31–51.

Drouin, M., Godard, M., Ildefonse, B., Bruguier, O. & Garrido, C. J. (2009). Geochemical and petrographic evidence for magmatic impregnation in the oceanic lithosphere at Atlantis Massif, Mid-Atlantic Ridge (IODP Hole U1309D, 30°N). *Chemical Geology* **264**, 71–88.

Escartín, J., Smith, D. K., Cann, J., Schouten, H., Langmuir, C. H. & Escrig, S. (2008). Central role of detachment faults in

Downloaded from https://academic.oup.com/petrology/article/61/9/egaa082/5890488 by Institute of Geology and Geophysics, CAS user on 04 March 2021

accretion of slow-spreading oceanic lithosphere. *Nature* **455**, 790.

Ferrando, C., Godard, M., Ildefonse, B. & Rampone, E. (2018). Melt transport and mantle assimilation at Atlantis massif (IODP site U1309): Constraints from geochemical modeling. *Lithos* **323**, 24–43.

Gao, Y., Hoefs, J., Hellebrand, E., Handt, A. V. D. & Snow, J. E. (2007). Trace element zoning in pyroxenes from ODP Hole 735B gabbros: diffusive exchange or synkinematic crystal fractionation? *Contributions to Mineralogy & Petrology* **153**, 429–442.

Georgen, J. E., Lin, J. & Dick, H. J. B. (2001). Evidence from gravity anomalies for interactions of the Marion and Bouvet hotspots with the Southwest Indian Ridge: effects of transform offsets. *Earth and Planetary Science Letters* **187**, 283–300.

Gillis, K. M. & Meyer, P. S. (2001). Metasomatism of oceanic gabbros by late stage melts and hydrothermal fluids: Evidence from the rare earth element composition of amphiboles. *Geochemistry Geophysics Geosystems* ***2***.

Godard, M., Awaji, S., Hansen, H., Hellebrand, E., Brunelli, D., Johnson, K., Yamasaki, T., Maeda, J., Abratis, M., Christie, D., Kato, Y., Mariet, C. & Rosner, M. (2009). Geochemistry of a long in-situ section of intrusive slow-spread oceanic lithosphere: Results from IODP Site U1309 (Atlantis Massif, 30°N Mid-Atlantic-Ridge). *Earth and Planetary Science Letters* **279**, 110–122.

Griffin, W., Powell, W., Pearson, N. & O'reilly, S. (2008). GLITTER: data reduction software for laser ablation ICP-MS. *Laser Ablation-ICP-MS in the earth sciences. Mineralogical association of Canada short course series* ***40***, 204–207.

Harding, A. J., Orcutt, J. A., Kappus, M. E., Vera, E. E., Mutter, J. C., Buhl, P., Detrick, R. S. & Brocher, T. M. (1989). Structure of young oceanic crust at 13°N on the East Pacific Rise from expanding spread profiles. *Journal of Geophysical Research Solid Earth* **94**, 12163–12196.

Harigane, Y., Okamoto, A., Morishita, T., Snow, J. E., Tamura, A., Yamashita, H., Michibayashi, K., Ohara, Y. & Arai, S. (2019). Melt–fluid infiltration along detachment shear zones in oceanic core complexes: Insights from amphiboles in gabbro mylonites from the Godzilla Megamullion, Parece Vela Basin, the Philippine Sea. *Lithos* **344–345**, 217–231.

Hart, S. R. & Dunn, T. (1993). Experimental cpx/melt partitioning of 24 trace elements. *Contributions to Mineralogy and Petrology* **113**, 1–8.

Hasalová, P., Štípská, P., Powell, R., Schulmann, K., Janoušek, V., &Lexa, O. (2008). Transforming mylonitic metagranite by open-system interactions during melt flow. *Journal of Metamorphic Geology*, **26**, 55–80.

Holness, M. B., Vukmanovic, Z. & Mariani, E. (2017). Assessing the Role of Compaction in the Formation of Adcumulates: a Microstructural Perspective. *Journal of Petrology* **58**, 643–673.

Holtzman, B. K. & Kohlstedt, D. L. (2007). Stress-driven Melt Segregation and Strain Partitioning in Partially Molten Rocks: Effects of Stress and Strain. *Journal of Petrology* **48**, 2379–2406.

Jochum, K. P., Nohl, U., Herwig, K., Lammel, E., Stoll, B. & Hofmann, A. W. (2005). GeoReM: A New Geochemical Database for Reference Materials and Isotopic Standards. *Geostandards & Geoanalytical Research* **29**, 333–338.

Kaczmarek, M.-A. & Müntener, O. (2008). Juxtaposition of Melt Impregnation and High-Temperature Shear Zones in the Upper Mantle; Field and Petrological Constraints from the Lanzo Peridotite (Northern Italy). *Journal of Petrology* **49**, 2187–2220.

Kelemen, P. B. & Dick, H. J. B. (1995). Focused melt flow and localized deformation in the upper mantle: Juxtaposition of replacive dunite and ductile shear zones in the Josephine peridotite, SW Oregon. *Journal of Geophysical Research: Solid Earth* **100**, 423–438.

Koepke, J., Botcharnikov, R. E. & Natland, J. H. (2018). Crystallization of late-stage MORB under varying water activities and redox conditions: Implications for the formation of highly evolved lavas and oxide gabbro in the ocean crust. *Lithos* **323**, 58–77.

Koepke, J., Feig, S. T., Snow, J. & Freise, M. (2004). Petrogenesis of oceanic plagiogranites by partial melting of gabbros: an experimental study. *Contributions to Mineralogy and Petrology* **146**, 414–432.

Leuthold, J., Lissenberg, C. J., O'Driscoll, B., Karakas, O., Falloon, T., Klimentyeva, D. N. & Ulmer, P. (2018). Partial Melting of Lower Oceanic Crust Gabbro: Constraints From Poikilitic Clinopyroxene Primocrysts. *Frontiers in Earth Science* **6**.

Lissenberg, C. J. & Dick, H. J. B. (2008). Melt–rock reaction in the lower oceanic crust and its implications for the genesis of mid-ocean ridge basalt. *Earth & Planetary Science Letters* **271**, 311–325.

Lissenberg, C. J. & Macleod, C. J. (2016). A Reactive Porous Flow Control on Mid-ocean Ridge Magmatic Evolution. *Journal of Petrology* **57**, 2195–2220.

Lissenberg, C. J., MacLeod, C. J. & Bennett, E. N. (2019). Consequences of a crystal mush-dominated magma plumbing system: a mid-ocean ridge perspective. *Philosophical Transactions of the Royal Society A: Mathematical, Physical and Engineering Sciences* **377**, 20180014.

Lissenberg, C. J., MacLeod, C. J., Howard, K. A. & Godard, M. (2013). Pervasive reactive melt migration through fast-spreading lower oceanic crust (Hess Deep, equatorial Pacific Ocean). *Earth and Planetary Science Letters* **361**, 436–447.

MacLeod, C. J., Dick, H. J. B., Blum, P., Abe, N., Blackman, D. K., Bowles, J. A., Cheadle, M. J., Cho, K., Ciazela, J., Deans, J. R., Edgcomb, V. P., Ferrando, C., France, L., Ghosh, B., Ildefonse, B. M., Kendrick, M. A., Koepke, J. H., Leong, J. A. M., Liu, C., Ma, Q., Morishita, T., Morris, A., Natland, J. H., Nozaka, T., Pluemper, O., Sanfilippo, A., Sylvan, J. B., Tivey, M. A., Tribuzio, R. & Viegas, L. G. F. (2017). Site U1473. *In MacLeod, C.J., Dick, H.J.B., Blum, P., and the Expedition 360 Scientists, Southwest Indian Ridge Lower Crust and Moho. Proceedings of the International Ocean Discovery Program*, **360**. College Station, TX (International Ocean Discovery Program).

Meek, U., Piazolo, S. & Daczko, N. R. (2019). The field and microstructural signatures of deformation-assisted melt transfer: Insights from magmatic arc lower crust, New Zealand. *Journal of Metamorphic Geology* **37**, 795–821.

Meurer, W. P. & Boudreau, A. E. (1998). Compaction of Igneous Cumulates Part II: Compaction and the Development of Igneous Foliations. *The Journal of Geology* **106**, 293–304.

Meyer, P. S., Dick, H. J. B. & Thompson, G. (1989). Cumulate gabbros from the Southwest Indian Ridge, 54°S-7° 16′ E: implications for magmatic processes at a slow spreading ridge. *Contributions to Mineralogy and Petrology* **103**, 44–63.

Natland, J. H. & Dick, H. J. B. (2001). Formation of the lower ocean crust and the crystallization of gabbroic cumulates at a very slowly spreading ridge. *Journal of Volcanology and Geothermal Research* **110**, 191–233.

Natland, J. H., Meyer, P. S., Dick, H. J. & Bloomer, S. H. (1991). Magmatic oxides and sulfides in gabbroic rocks from Hole

Downloaded from https://academic.oup.com/petrology/article/61/9/egaa082/5890488 by Institute of Geology and Geophysics, CAS user on 04 March 2021

735B and the later development of the liquid line of descent. *In Von Herzen, RP, Robinson, PT, et al., Proc. ODP, Sci. Results*, 75–111.

Olive, J.-A., Behn, M. D. & Tucholke, B. E. (2010). The structure of oceanic core complexes controlled by the depth distribution of magma emplacement. *Nature Geoscience* **3**, 491–495.

Pearce, N. J. G., Perkins, W. T., Westgate, J. A., Gorton, M. P., Jackson, S. E., Neal, C. R. & Chenery, S. P. (1997). A Compilation of New and Published Major and Trace Element Data for NIST SRM 610 and NIST SRM 612 Glass Reference Materials. *Geostandards Newsletter* **21**, 115–144.

Rampone, E., Borghini, G., Godard, M., Ildefonse, B., Crispini, L. & Fumagalli, P. (2016). Melt/rock reaction at oceanic peridotite/gabbro transition as revealed by trace element chemistry of olivine. *Geochimica et Cosmochimica Acta* **190**, 309–331.

Sanfilippo, A., Dick, H. J. B., Marschall, H. R., Lissenberg, C. J. & Urann, B. (2018). Emplacement and high-temperature evolution of gabbros of the 16.5 °N oceanic core complexes (Mid-Atlantic Ridge): insights into the compositional variability of the lower oceanic crust. *Geochemistry, Geophysics, Geosystems* **20**, 46–66.

Sanfilippo, A., Dick, H. J. B., Ohara, Y. & Tiepolo, M. (2016). New insights on the origin of troctolites from the breakaway area of the Godzilla Megamullion (Parece Vela back-arc basin): The role of melt-mantle interaction on the composition of the lower crust. *Island Arc* **25**, 220–234.

Sanfilippo, A., Morishita, T., Kumagai, H., Nakamura, K., Okino, K., Hara, K., Tamura, A. & Arai, S. (2015a). Hybrid troctolites from mid-ocean ridges: inherited mantle in the lower crust. *Lithos* **232**, 124–130.

Sanfilippo, A., Tribuzio, R. & Tiepolo, M. (2014). Mantle–crust interactions in the oceanic lithosphere: Constraints from minor and trace elements in olivine. *Geochimica et Cosmochimica Acta* **141**, 423–439.

Sanfilippo, A., Tribuzio, R., Tiepolo, M. & Berno, D. (2015b). Reactive flow as dominant evolution process in the lowermost oceanic crust: evidence from olivine of the Pineto ophiolite (Corsica). *Contributions to Mineralogy and Petrology* **170**, 38.

She, Y.-W., Song, X.-Y., Yu, S.-Y. & He, H.-L. (2015). Variations of trace element concentration of magnetite and ilmenite from the Taihe layered intrusion, Emeishan large igneous province, SW China: Implications for magmatic fractionation and origin of Fe–Ti–V oxide ore deposits. *Journal of Asian Earth Sciences* **113**, 1117–1131.

Sinton, J. M. & Detrick, R. S. (1992). Mid-ocean ridge magma chambers. *Journal of Geophysical Research Solid Earth* **97**, 197–216.

Smith, D. K., Cann, J. R. & Escartín, J. (2006). Widespread active detachment faulting and core complex formation near 13° N on the Mid-Atlantic Ridge. *Nature* **442**, 440–443.

Spandler, C. & O'Neill, H. S. C. (2010). Diffusion and partition coefficients of minor and trace elements in San Carlos olivine at 1,300°C with some geochemical implications. *Contributions to Mineralogy & Petrology* **159**, 791–818.

Suhr, G., Hellebrand, E., Johnson, K. & Brunelli, D. (2008). Stacked gabbro units and intervening mantle: A detailed look at a section of IODP Leg 305, Hole U1309D. *Geochemistry Geophysics Geosystems* **9**, 196–199.

Sun, C., Graff, M. & Liang, Y. (2017). Trace element partitioning between plagioclase and silicate melt: The importance of temperature and plagioclase composition, with implications for terrestrial and lunar magmatism. *Geochimica et Cosmochimica Acta* **206**, 273–295.

Sun, C. & Liang, Y. (2012). Distribution of REE between clinopyroxene and basaltic melt along a mantle adiabat: effects of major element composition, water, and temperature. *Contributions to Mineralogy and Petrology* **163**, 807–823.

Sun, C. & Liang, Y. (2013a). Distribution of REE and HFSE between low-Ca pyroxene and lunar picritic melts around multiple saturation points. *Geochimica et Cosmochimica Acta*, **119**, 340–358.

Sun, C. & Liang, Y. (2013b). The importance of crystal chemistry on REE partitioning between mantle minerals (garnet, clinopyroxene, orthopyroxene, and olivine) and basaltic melts. *Chemical Geology*, **358**, 23–36.

Sun, C. & Liang, Y. (2017). A REE-in-plagioclase–clinopyroxene thermometer for crustal rocks. *Contributions to Mineralogy and Petrology* **172**, 24.

Sun, C. & Lissenberg, C. J. (2018). Formation of fast-spreading lower oceanic crust as revealed by a new Mg–REE coupled geospeedometre. *Earth and Planetary Science Letters* **487**, 165–178.

Sun, S. S. & Mcdonough, W. F. (1989). Chemical and isotopic systematics of oceanic basalts: implications for mantle composition and processes. *Geological Society London Special Publications* **42**, 313–345.

Tribuzio, R., Manatschal, G., Renna, M. R., Ottolini, L. & Zanetti, A. (2020). Tectono-magmatic interplay and related metasomatism in gabbros from the Chenaillet ophiolite (Western Alps). *Journal of Petrology*.

Tucholke, B. E., Behn, M. D., Buck, W. R. & Lin, J. (2008). Role of melt supply in oceanic detachment faulting and formation of megamullions. *Geology* **36**, 455–458.

Tucholke, B. E., Lin, J. & Kleinrock, M. C. (1998). Megamullions and mullion structure defining oceanic metamorphic core complexes on the Mid-Atlantic Ridge. *Journal of Geophysical Research Solid Earth* **103**, 9857–9866.

Wu, S.-T., Huang, C., Xie, L.-W., Yang, Y.-H. & Yang, J.-H. (2018a). Iolite Based Bulk Normalization as 100% (m/m) Quantification Strategy for Reduction of Laser Ablation-Inductively Coupled Plasma-Mass Spectrometry Transient Signal. *Chinese Journal of Analytical Chemistry* **46**, 1628–1636.

Wu, S., Karius, V., Schmidt, B. C., Simon, K. & Wörner, G. (2018b). Comparison of Ultrafine Powder Pellet and Flux-free Fusion Glass for Bulk Analysis of Granitoids by Laser Ablation-Inductively Coupled Plasma-Mass Spectrometry. *Geostandards and Geoanalytical Research* **42**, 575–591.

Yang, A.Y., Wang, C., Liang, Y., Lissenberg, C.J. (2019). Reaction Between Mid-Ocean Ridge Basalt and Lower Oceanic Crust: An Experimental Study. *Geochemistry, Geophysics, Geosystems*, **20**, 4390–4407.

Yao, L., Sun, C., Liang, Y. (2012). A parametreized model for REE distribution between low-Ca pyroxene and basaltic melts with applications to REE partitioning in low-Ca pyroxene along a mantle adiabat and during pyroxenite-derived melt and peridotite interaction. *Contributions to Mineralogy and Petrology*, **164**, 261–280.

Yu, X. & Dick, H. J. B. (2020). Plate-driven micro-hotspots and the evolution of the Dragon Flag melting anomaly, *Southwest Indian Ridge. Earth and Planetary Science Letters* **531**, 116002.

Downloaded from https://academic.oup.com/petrology/article/61/9/egaa082/5890488 by Institute of Geology and Geophysics, CAS user on 04 March 2021